Ore Geology Reviews 183 (2025) 106701



Contents lists available at ScienceDirect

Ore Geology Reviews

journal homepage: www.elsevier.com/locate/oregeorev





Remote sensing and aeromagnetic data integration for mapping Cu, Mn, Co, Ba, and Fe Mineralization: A Case study from Aït Semgane, Anti-Atlas, Morocco

Mohamed Ali El-Omairi [a], Abdelkader El Garouani [a], Mahmoud Abdellatif [b], Manal El Garouani [a], Mohammed Boumehdi [c], Ali Shebl [d,e,*]

[a] Geo-Resources and Environment Laboratory, Sidi Mohamed Ben Abdellah University, FST-Fez, P.O. Box, 2202, Fez 30000, Morocco
[b] Department of Geology, South Valley University, Qena 83523, Egypt
[c] National Office of Hydrocarbons and Mines, Rabat, Morocco
[d] Department of Geology, Tanta University, Tanta 31527, Egypt
[e] Department of Mineralogy and Geology, University of Debrecen, Debrecen 4032, Hungary

ARTICLE INFO

Keywords:
Mineral exploration
Remote sensing
Hydrothermal alteration
Structural controls
Spectral indices
Anti-Atlas Morocco

ABSTRACT

This study presents a comprehensive exploration of mineralization patterns in the Aït Semgane region of the Anti-Atlas, Morocco, through the integration of remote sensing (Sentinel-2 and PRISMA hyperspectral data), aeromagnetic surveys, field observations and petrographic investigations. The study reveals strong spatial correlations between spectral anomalies, lithological formations, and tectonic structures, highlighting the geological controls on the distribution of copper, manganese, cobalt, baryte, and iron mineralization. Sentinel-2 spectral indices identified key anomalies aligned with major faults and shear zones, particularly within volcanosedimentary (NP3, NP2) and Ouarzazate Group formations, suggesting hydrothermal fluid circulation as a primary mineralization mechanism. PRISMA hyperspectral data enhanced lithological mapping and hydrothermal alteration detection, with spectral analysis Sequential Maximum Angle Convex Cone (SMACC), independent component analysis (ICA), and constrained energy minimization (CEM) techniques identifying alteration minerals and minerals associated with the mineralized zones such as serpentine, baryte, chalcopyrite, and iron oxides. Aeromagnetic data analysis revealed a highly deformed structural framework, with NE-SW, NW-SE, E-W, and N-S trending magnetic anomalies, further corroborating the structural control on mineralization. Field validation confirmed the presence of mineralization in predicted zones, with microscopic analysis revealing mineralogical associations such as malachite, pyrolusite, cobaltite, and hematite. Despite the effectiveness of the integrated approach, the spectral resolution of Sentinel-2 and the limited availability of extensive geochemical datasets suggest opportunities for further refinement. Future detailed remote sensing analysis and advanced geophysical investigations could enhance the accuracy and depth of exploration of the explored zones. This study underscores the value of multidisciplinary data integration for efficient mineral exploration and provides a robust framework for sustainable resource development in structurally complex terrains.

1. Introduction

The exploration of mineral resources, particularly strategic metals such as iron, copper, cobalt, manganese, and Baryte, is critical for supporting global industrial development and the transition to green technologies. These minerals are the backbone of countless applications, from building infrastructure and powering energy storage systems to enabling advanced electronics and renewable energy solutions (Harben and Kužvart, 1997); "Mineral Commodity Summaries 2023," 2023; EL-Omairi and El Garouani, 2023;). However, traditional exploration methods—such as field surveys, drilling, and geochemical sampling are often expensive, time-consuming, and can have significant environmental impacts (Moon et al., 2009; (Gonzalez-Alvarez et al., 2020). To tackle these challenges, modern techniques like remote sensing and integrated geophysical-geochemical approaches have emerged as game-changers, offering more efficient and sustainable ways to explore for

* Corresponding author at: Department of Mineralogy and Geology, University of Debrecen, Debrecen 4032, Hungary.
E-mail addresses: ali.shebl@science.tanta.edu.eg, alishebl@mailbox.unideb.hu (A. Shebl).

https://doi.org/10.1016/j.oregeorev.2025.106701
Received 26 February 2025; Received in revised form 24 May 2025; Accepted 24 May 2025
Available online 26 May 2025
0169-1368/© 2025 The Author(s). Published by Elsevier B.V. This is an open access article under the CC BY-NC license (http://creativecommons.org/licenses/by-nc/4.0/).

Table 1
Sentinel-2 spectral indices for mineral mapping.

Index	Formula	Target Minerals	Geological Context	Key References
Cu	B12/B2	Cu-carbonates, sulfides	Hydrothermal alteration zones	(Sillitoe, 2010)
Mn	B8A/B3	Mn-oxides	Stratiform/ supergene deposits	(Maynard, 2012)
Co	B8/B4	Co-arsenides	Serpentinized ultramafics	(Evans, 2012)
Ba	B11/B2	Baryte	Hydrothermal veins	(Bedini, 2017)
Fe	B11/B4	Fe-oxides	Gossans, oxidation zones	(Hunt and Ashley, 1979)

minerals (Ali EL-Omairi et al., 2024).

In this study, we're taking advantage of cutting-edge technology by using multispectral data from Sentinel-2 and hyperspectral data from PRISMA to analyze the geological and hydrothermal features of our study area. Launched in 2019, the PRISMA satellite provides incredibly detailed hyperspectral imagery, allowing us to detect subtle mineral variations that would otherwise go unnoticed with traditional multispectral sensors (Shebl et al., 2023). These advanced datasets have already proven their worth in various fields, from mapping rock types (El-Omairi et al., 2025; Shebl et al., 2022; Van Der Meer et al., 2012); Ait (Ali et al., 2025; Choukrad et al., 2022; Ez-Zghoudy et al., 2023); to analyzing land use and mineral composition(Aplin, 2004; Adiri et al., 2017; Liu, 2015; Liu et al., 2023; Ait Ali et al., 2024). By combining PRISMA and Sentinel-2 data, we can gain a deeper understanding of surface and near-surface mineral distributions, helping us pinpoint potential mineralization zones with greater accuracy. (See Table 1.).

To complement this, we've also used aeromagnetic data to map out key geological structures linked to mineralization(Telford et al., 1990). Using advanced processing techniques like Reduction to the Pole (RTP) and Euler Deconvolution, we've been able to enhance our interpretation of these structures, giving us a clearer picture of where minerals might be concentrated. Such structural features have been shown to exert a strong control on hydrothermal mineralization in nearby regions, as demonstrated by (Salmi et al., 2024) in the Ousdrat and Aït Ahmane ore deposits of the Bou Azzer-El Graara inlier.

The heart of this study addresses a pressing challenge: the need for more efficient and precise methods to identify and map mineral deposits, especially in geologically complex regions like the Aït Semgane

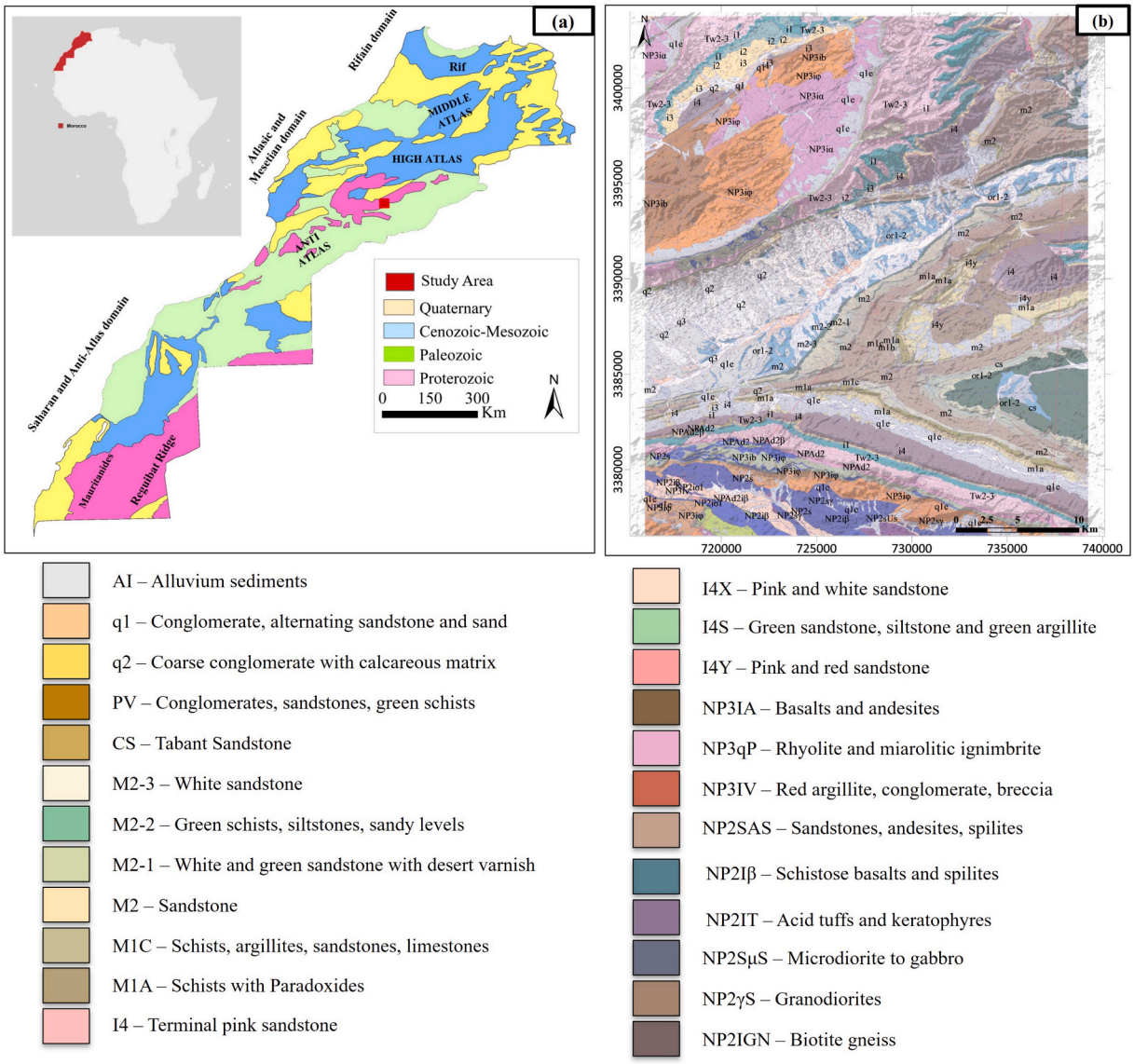


Fig. 1. A) Geographical location of the study area, b) Geological map of the study area, adapted from (Yazidi et al., 2008).

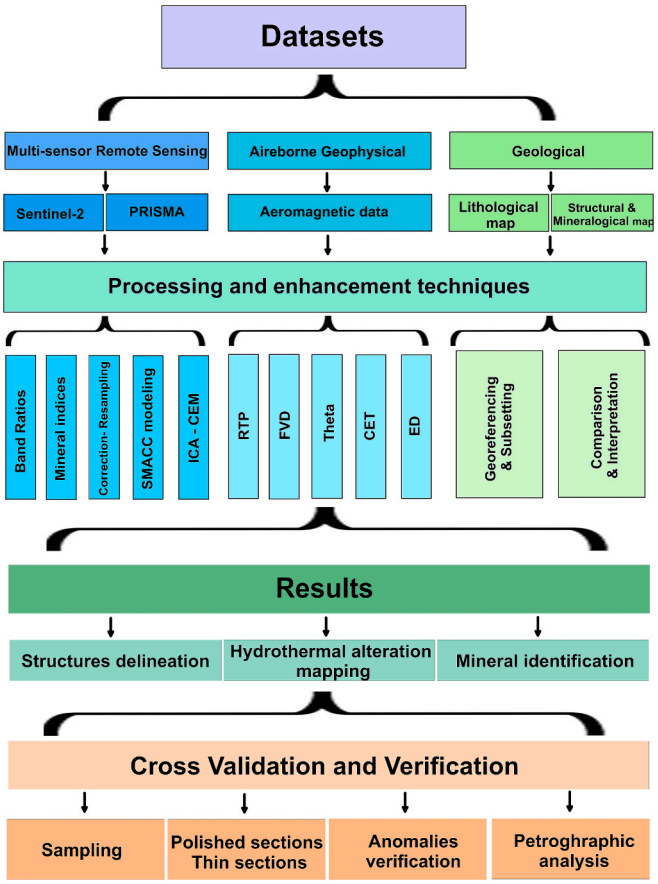


Fig. 2. Flowchart depicting the methodology applied in this research.

area. While traditional methods are reliable, they often fall short in providing comprehensive coverage and can be prohibitively expensive for large-scale projects (Gonzalez-Alvarez et al., 2020). That's why we're proposing an integrated approach that combines remote sensing, geophysics, and petrographic analysis to overcome these limitations.

The primary goal of this research is to develop a robust, multidisciplinary framework for mineral exploration in the Aït Semgane region by integrating cutting-edge remote sensing techniques, geophysical surveys, and ground-truth validation. Specifically, this study aims to:

Characterize the spatial distribution of key mineralizations (Cu, Mn, Co, Ba, Fe) using advanced spectral indices derived from Sentinel-2 multispectral and PRISMA hyperspectral data.

Decipher the structural controls on mineralization by analyzing aeromagnetic data (e.g., RTP, FVD, Euler deconvolution) to map faults, shear zones, and lithological contacts.

Validate the results through field missions, including sampling of mineralized zones and petrographic analysis using polished sections.

Assess the limitations and scalability of the integrated approach, compare the effectiveness of Sentinel-2 (medium resolution) vs. PRISMA (high resolution) for mineral mapping, and propose guidelines for future exploration in similar terrains.

What sets this study apart is its innovative, multi-source approach to mineral exploration a first for this region. While most research tends to focus on a single method, we're combining remote sensing, geophysics, and geochemistry to maximize the accuracy and reliability of our results. Additionally, our focus on strategic, high-value minerals aligns with the growing demand for resources essential to modern technologies and the global energy transition.

Ultimately, this research aims to showcase the power of an integrated approach to mineral exploration, offering more efficient and sustainable tools for discovering and managing mineral resources. The findings could have far-reaching implications for the mining industry, helping to optimize exploration strategies and support the responsible use of these critical materials.

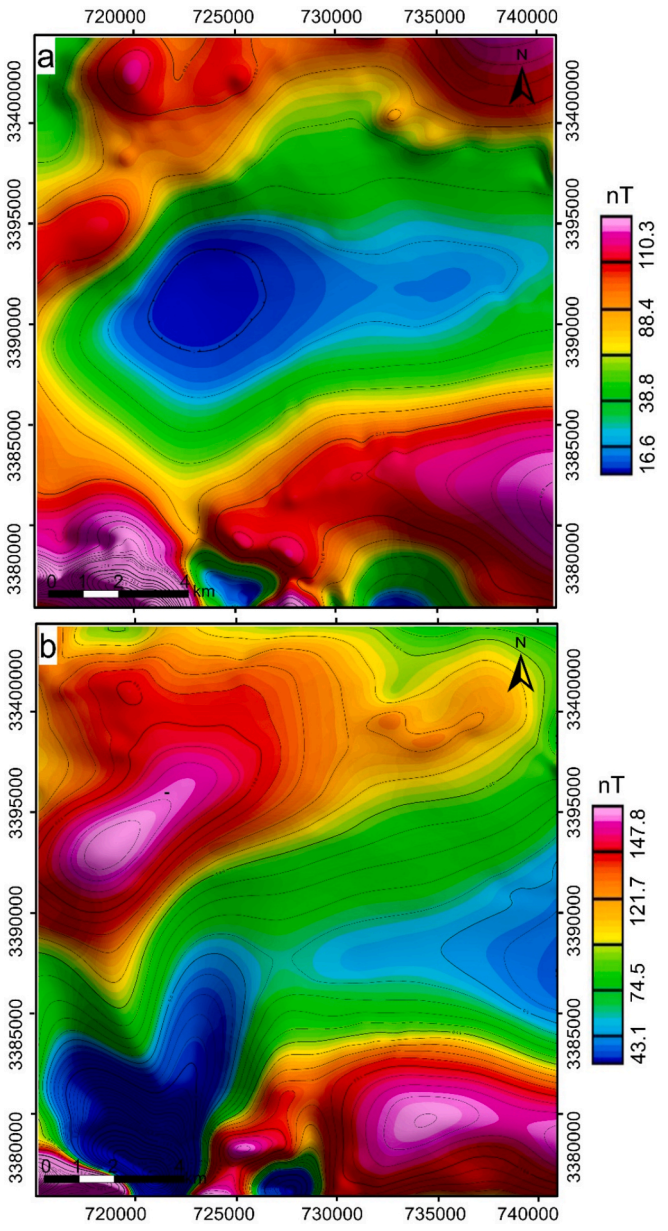


Fig. 3. Aeromagnetic data a) Total magnetic intensity (TMI) b) Reduced to pole (RTP) map.

2. Study area

Our study area is nestled in the southeastern part of Ouarzazate, within the central Anti-Atlas region, and covers the 1:50,000-scale topographic map of Aït Semgane. It stretches between latitudes 31°30′N and 31°45′N and longitudes 6°30′W and 6°45′W. This region is a geologist's dream, offering a stunning mix of rugged terrain and dramatic landscapes.

At the heart of the area lies the Jbel Saghro mountain range, where peaks soar to over 2,500 m, creating a striking backdrop. The landscape is shaped by extensive granitic and volcanic formations, giving it a rugged and varied character. In the central part of the region, you'll find

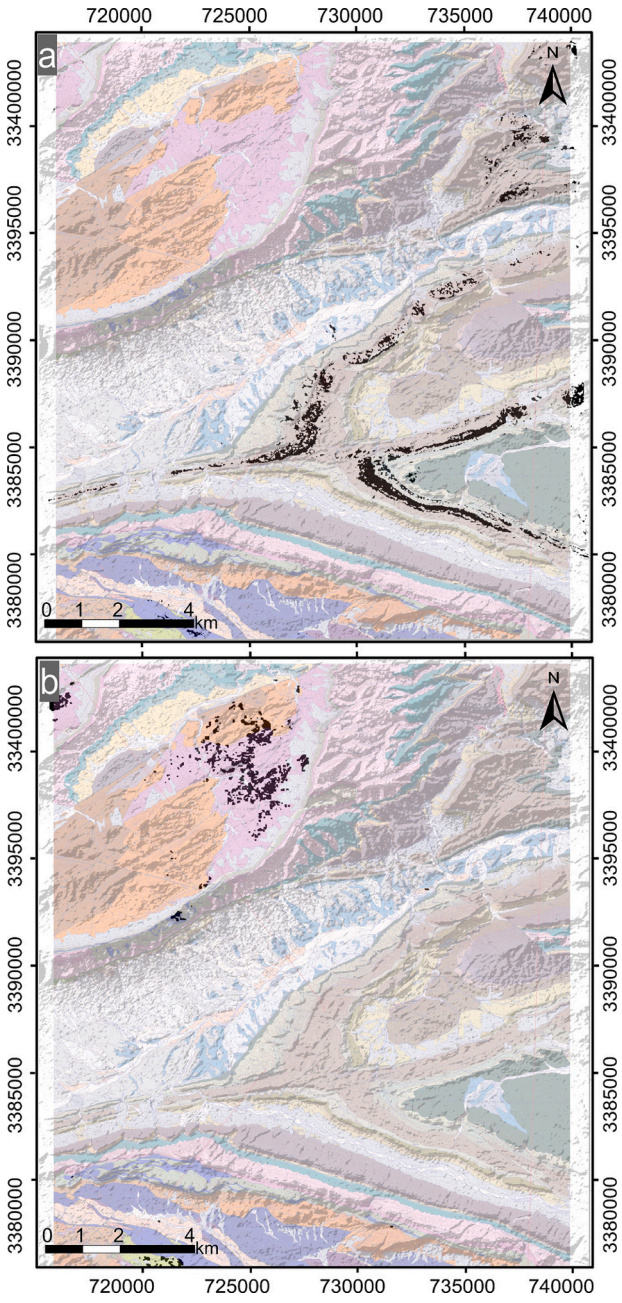


Fig. 4. (a) Copper (black) index anomaly map, (b) Manganese (black) index anomaly map;

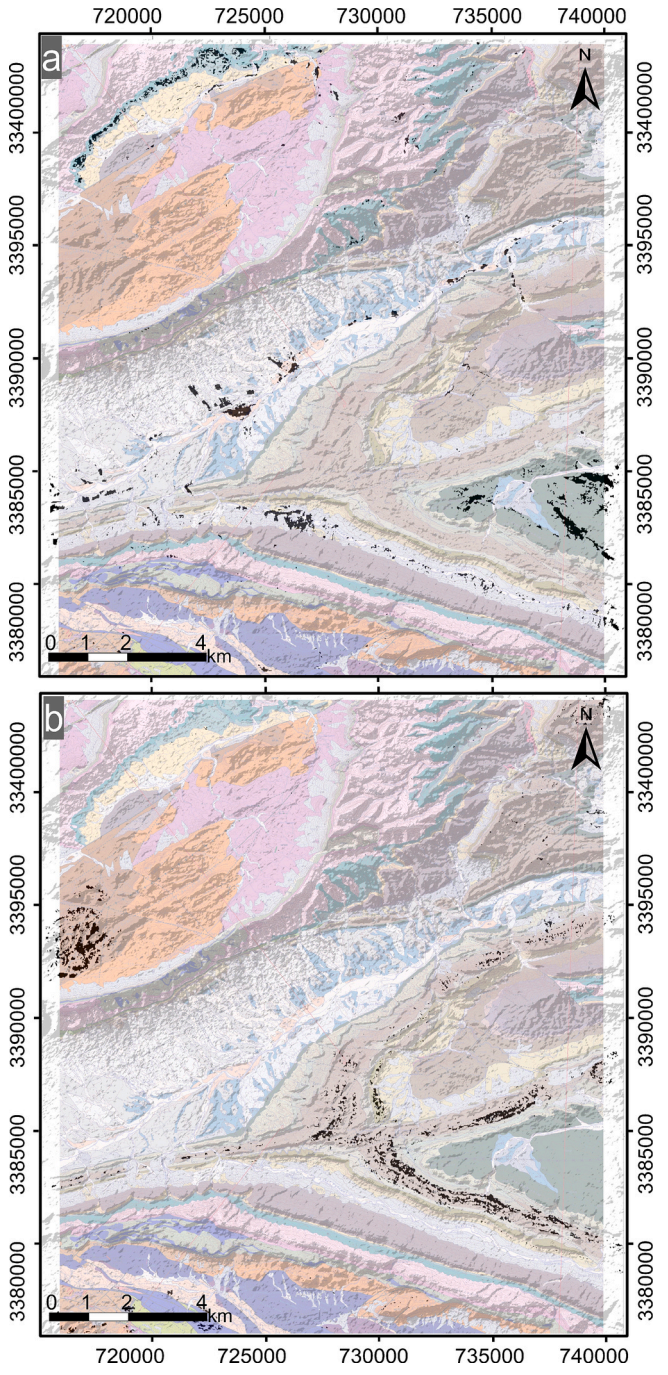


Fig. 5. (a) Cobalt index anomaly map, (b) Baryte index anomaly map.

mountainous plains (1,300–1,500 m in elevation), dotted with dome-shaped massifs and inselbergs—isolated hills that rise abruptly from the surrounding plains. Meanwhile, the outer edges of the area transition into a Saharan-type landscape, featuring valleys and basins carved out by the region's arid climate and occasional water flows. These basins are often framed by resistant rock formations like limestones and quartzites, adding to the area's geological diversity (Riser, 1988; Bajja, 1987; Abdelkareem et al., 2020).

Geologically, the Anti-Atlas region is a fascinating area located at the northern edge of the West African Craton. Over billions of years, it has been shaped by several major mountain-building events, known as orogenies, including the Eburnean, Pan-African, and Hercynian orogenies. These events span an incredible timeline, from the Paleoproterozoic era to the Paleozoic era (Blein et al., 2011). The middle and upper Neoproterozoic formations (referred to as NP2i, NP2s, NP3i, and NP3s) are particularly interesting. They consist of a mix of volcanic rocks, granites, conglomerates, sandstones, and schists, marked by clear unconformities gaps in the geological record that tell stories of ancient erosion or tectonic activity (Fig. 1). Moving forward in time, the Paleozoic era left behind a post-Ediacaran sedimentary cover, including Lower Cambrian and Ordovician formations. These are made up of conglomerates, sandstones, dolomites, and even basalts, painting a vivid picture of the region's ancient environments (Walsh et al., 2012). More recently, during the Quaternary period, the region has been shaped by cycles of erosion and deposition, driven by climatic changes. These processes have created alluvial terraces and alluvial fans, which are like geological fingerprints, capturing the dynamic history of the area (Bajja, 1987). Together, these layers and features tell the story of a region that has been constantly reshaped by the forces of nature over hundreds of millions of years.

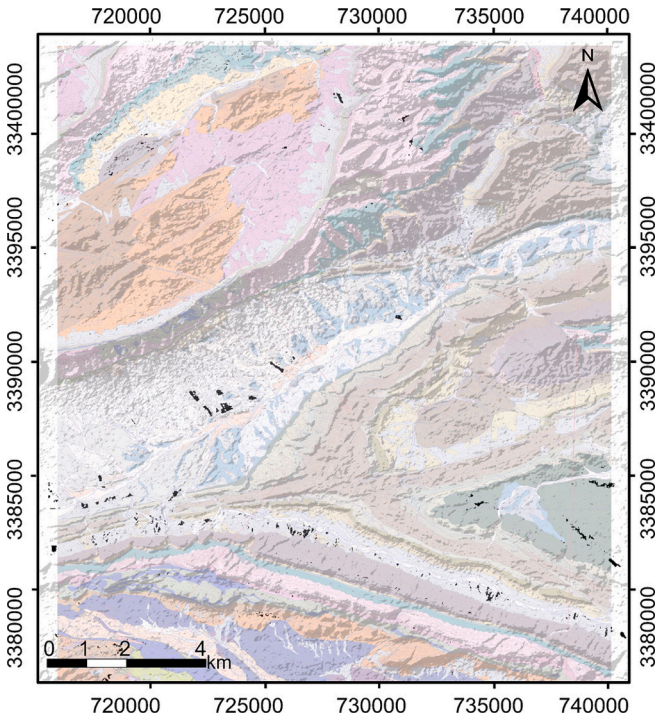


Fig. 6. Iron index anomaly map.

The area exhibits a diversity of metallic mineralizations, primarily concentrated within ophiolitic and volcanic formations. Cobalt deposits, located in the Bou Azzer district, are associated with Neoproterozoic (NP2i) serpentinites and occur as cobalt-rich arsenide and sulfo-arsenide veins, with accessory minerals such as gold, silver, and bismuth (Maacha et al., 2012). Copper and manganese, on the other hand, are found within the volcanic formations of the Lower Ouarzazate Group (NP3i), forming hydrothermal veins hosted in rhyolites and andesites. These mineral resources, either actively exploited or under exploration, highlight the metallogenic potential of the region and its economic significance for the mining industry (Walsh et al., 2012).

The Aït Semgane region was chosen for this study for several compelling reasons. First, its incredible geological diversity—featuring both Neoproterozoic and Paleozoic formations—makes it a perfect natural laboratory for testing and refining remote sensing and lithological mapping techniques. The area boasts a rich mix of volcanic, granitic, sedimentary, and magmatic rocks, offering a unique opportunity to compare and evaluate different classification methods and geological feature extraction approaches. Second, the region's climate and environmental conditions add another layer of interest. Cycles of erosion and river-driven deposition have shaped the landscape over time, providing a dynamic setting to study how landforms evolve and how geological processes continue to unfold. These conditions are especially valuable for testing how well remote sensing methods can capture a wide variety of geological and geomorphological features, even in challenging environments. Finally, the practical side of things also played a role in our decision. The area is accessible via local roads, and the presence of nearby communities not only makes fieldwork more feasible but also enriches the research experience. This accessibility allows us to ground-truth our remote sensing findings with real-world observations, ensuring the accuracy and reliability of our results.

3. Data used

In this study, we're using cutting-edge remote sensing data to uncover the secrets of the Aït Semgane region. One of the key tools in our toolkit is hyperspectral imagery from the PRISMA satellite, which has been available since 2019. What makes PRISMA so powerful is its high spectral resolution, allowing us to detect and analyze minerals and hydrothermal alterations in incredible detail. This capability gives us a deeper understanding of the mineralogical makeup of the area.

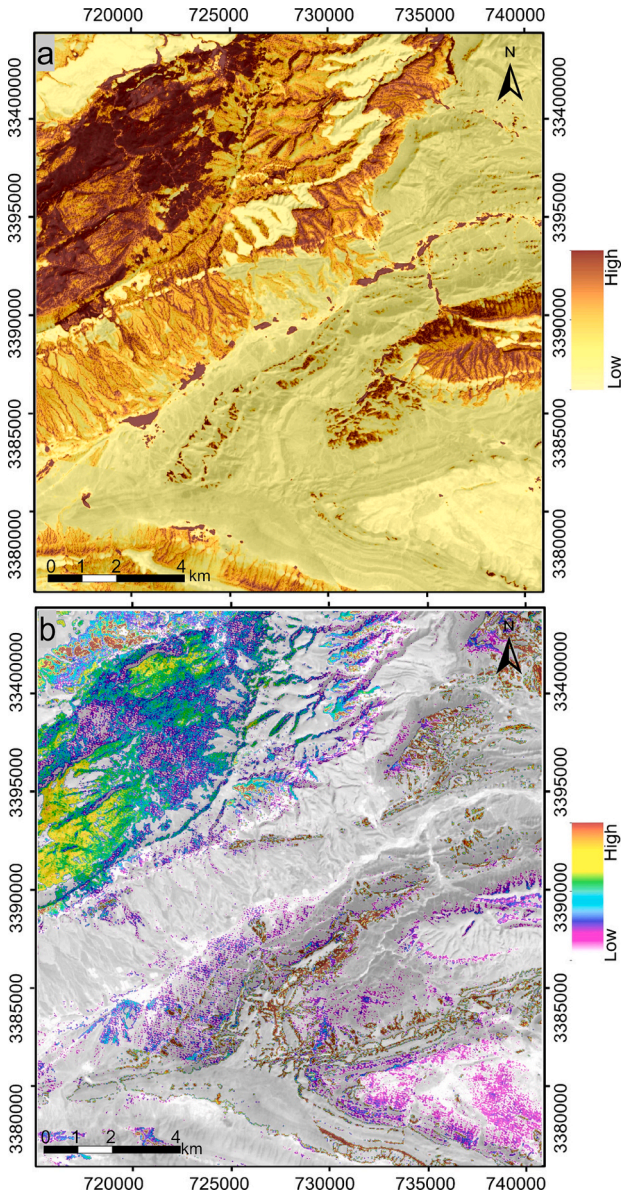


Fig. 7. (a) Endmember 2 abundance map showing three iron-bearing zones: northwestern (NP3 formation), southern (NP2 formation, metamorphosed mafic/ultramafic rocks), and central area. (b) Endmember 3 pseudocolor ramp highlighting spectral variations due to varied lithologies and alteration intensity.

PRISMA data comes in different levels, each serving a specific purpose. At Level 0, we get basic instrument and satellite data, like cloud cover percentages, stored in binary files. Moving up to Level 1, we find panchromatic radiance imagery (captured in the upper atmosphere) and hypercubes essentially 3D datasets that have been geometrically and radiometrically corrected for accuracy. Level 2 is where things get even more interesting. It's divided into four sub-levels: L2A: Provides geolocated ground-level reflectance images. L2B (Offers geolocated radiance images). L2C (Delivers geolocated reflectance images). L2D (Includes additional processed data for specific applications). These levels help us tailor the data to our needs, whether we're mapping surface reflectance, analyzing radiance, or pinpointing specific mineralogical features (Shaik et al., 2023); Shebl et al., 2023). This study

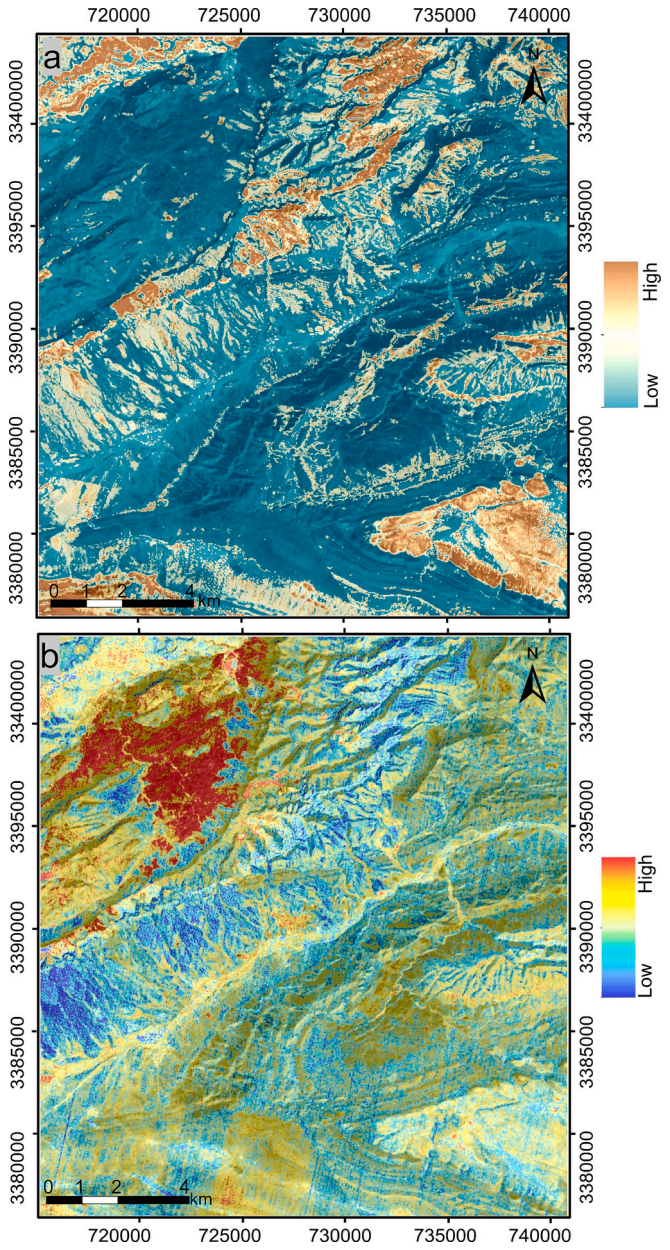


Fig. 8. (a) Endmember 9 pseudocolor ramp showing spectral variations and alteration. (b) ICA results highlighting NP3 rocks in the northwest (red), with scattered pixels in the west and south (NP2/NP3) associated with alteration and mineralization, correlating with Sentinel-2 anomalies. (For interpretation of the references to color in this figure legend, the reader is referred to the web version of this article.)

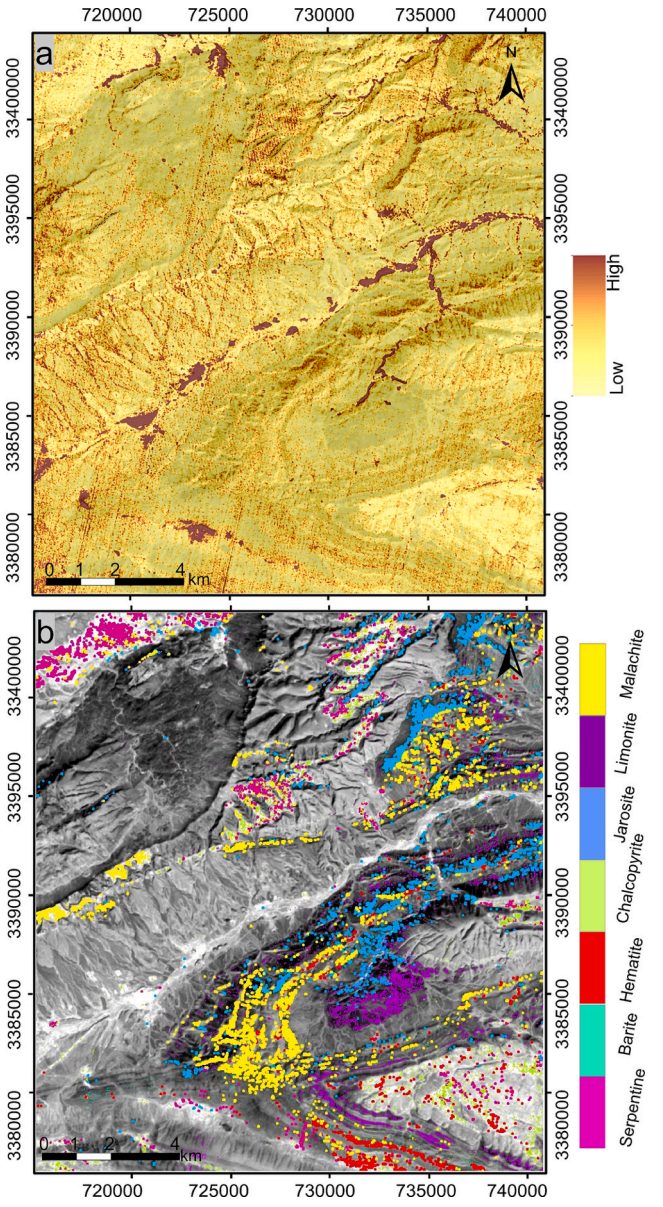


Fig. 9. (a) IC3 results showing three main hydrothermally altered zones (northwestern, NE-SW, southwestern) and widespread scattered alteration. The NNE-SSW striping visible is a noise in the original PRISMA data. It was not fully removed as doing so might obscure subtle target features within the image (b) CEM results are shown over grayscale PRISMA band 49 for clearer visualization.

utilized Level-2D data, which is pre-processed and ready for analysis. All available spectral bands were employed to support the research objectives and to provide a clearer understanding of the geological and mineralogical framework of the study area.

Additionally, multispectral Sentinel-2 imagery, acquired from the European Space Agency (ESA), was utilized. The imagery includes 13 spectral bands with spatial resolutions ranging from 10 m to 60 m. Key bands selected for mineralogical analysis include B2 (Blue, 490 nm), B3 (Green, 560 nm), B4 (Red, 665 nm), B8 (NIR, 842 nm), B11 (SWIR1, 1610 nm), and B12 (SWIR2, 2190 nm).

The primary remote sensing data consists of PRISMA hyperspectral imagery acquired on 07 October 2021 (0 % cloud cover, L2D surface reflectance product) and Sentinel-2B multispectral data from 25 October 2023 (0 % cloud cover, L1C Top-of-Atmosphere product). The PRISMA dataset provides 239 spectral bands between 400–2500 nm at 30 m spatial resolution, enabling detailed mineral identification.

Aeromagnetic data was conducted in 1999 as part of the National Geological Mapping Program (PNCG) and carried out by Fugro. The survey covered an area of approximately 82,152 km^2, with flight line spacing ranging from 500 to 600 m and oriented along azimuths of 15°, 30°, and 315°. Total magnetic field measurements were acquired using cesium vapor magnetometers (Scintrex CS-2 or Geometrics G822-A) mounted beneath a helicopter, maintaining a nominal flight altitude of 30 m above ground level. Diurnal variations were corrected using base station recordings. The magnetic data were subsequently interpolated onto a regular grid using appropriate geostatistical methods (e.g., kriging), with spatial resolution adapted to the flight line density. The processed data, delivered in GRD format, were used to generate magnetic anomaly maps for structural analysis and mineral exploration

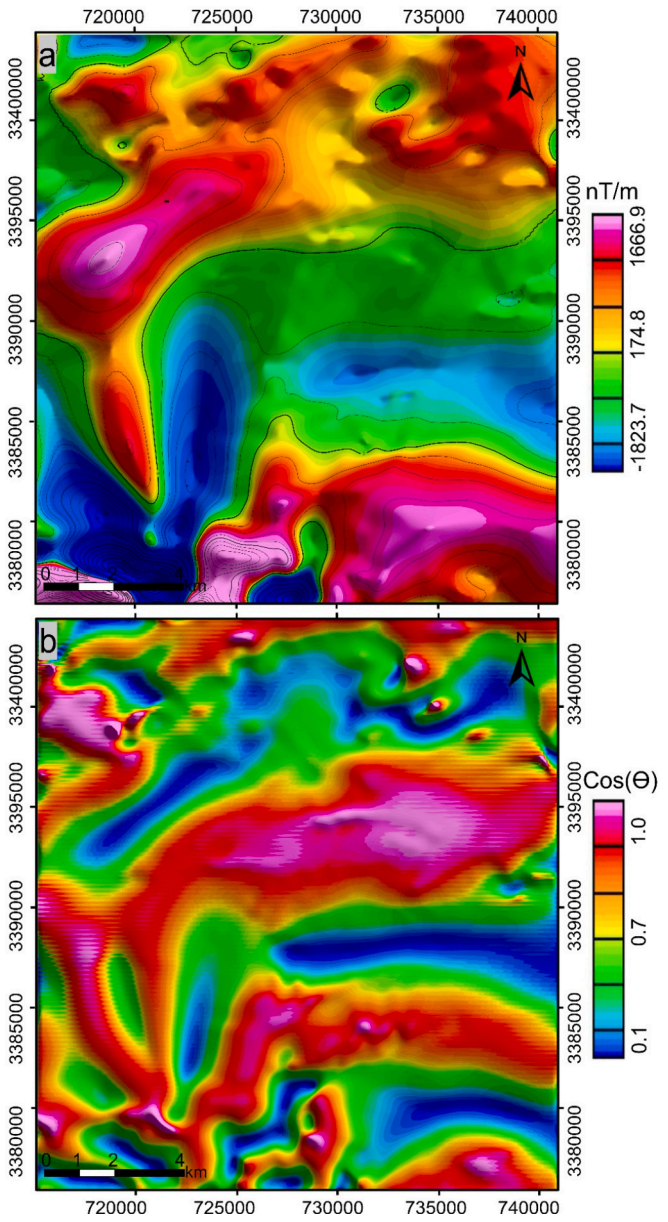


Fig. 10. Derivative maps a) First vertical derivative map, b) Theta map.

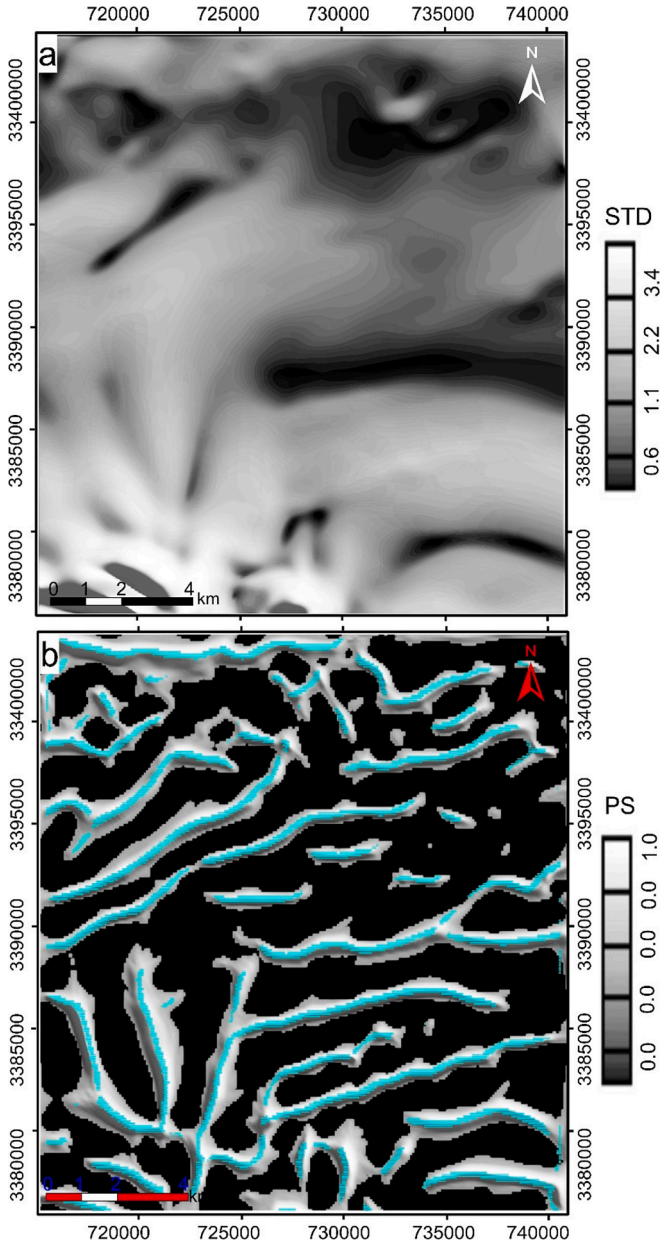


Fig. 11. CET grid analysis results a) Standard Deviation map, b) Phase symmetry map overlaid by Threshold results.

purposes.

Field missions were conducted to collect representative samples from various mineralization types observed in the study area. These samples were prepared as polished thin sections for detailed microscopic analysis, allowing for the identification of opaque mineral phases and determination of their chemical composition using Scanning Electron Microscopy (SEM) coupled with Energy Dispersive Spectroscopy (EDS).

Other complementary data include topographic information sourced from the Aït Semgane 1:50,000 map, which was used to contextualize the geological and geomorphological findings. Additionally, existing geological maps and previous studies of the region provided valuable information on the lithological formations and tectonic structures.

4. Methodology

The methodology of this study is based on an integrated approach, combining remote sensing data processing (Sentinel-2 and PRISMA), aeromagnetic geophysical data analysis, and field validations. These steps enable the identification and characterization of target minerals and associated geological structures, as illustrated in Fig. 2.

4.1. Remote sensing data processing

4.1.1. Acquisition and Preprocessing of Sentinel-2 image

Sentinel-2 images, obtained from the European Space Agency (ESA), consist of 13 spectral bands with spatial resolutions ranging from 10 m to 60 m. The bands selected for mineralogical analysis are as follows:

- B2 (Blue, 490 nm): Sensitive to variations in altered minerals.
- B3 (Green, 560 nm): Useful for identifying iron oxides and hydroxyl-bearing minerals.
- B4 (Red, 665 nm): Sensitive to the absorption of metallic oxides.
- B8 (Near-Infrared, 842 nm): Helps distinguish areas rich in ferruginous minerals.
- B11 (SWIR1, 1610 nm) & B12 (SWIR2, 2190 nm): Crucial for differentiating hydrothermal minerals and metallic sulfides.

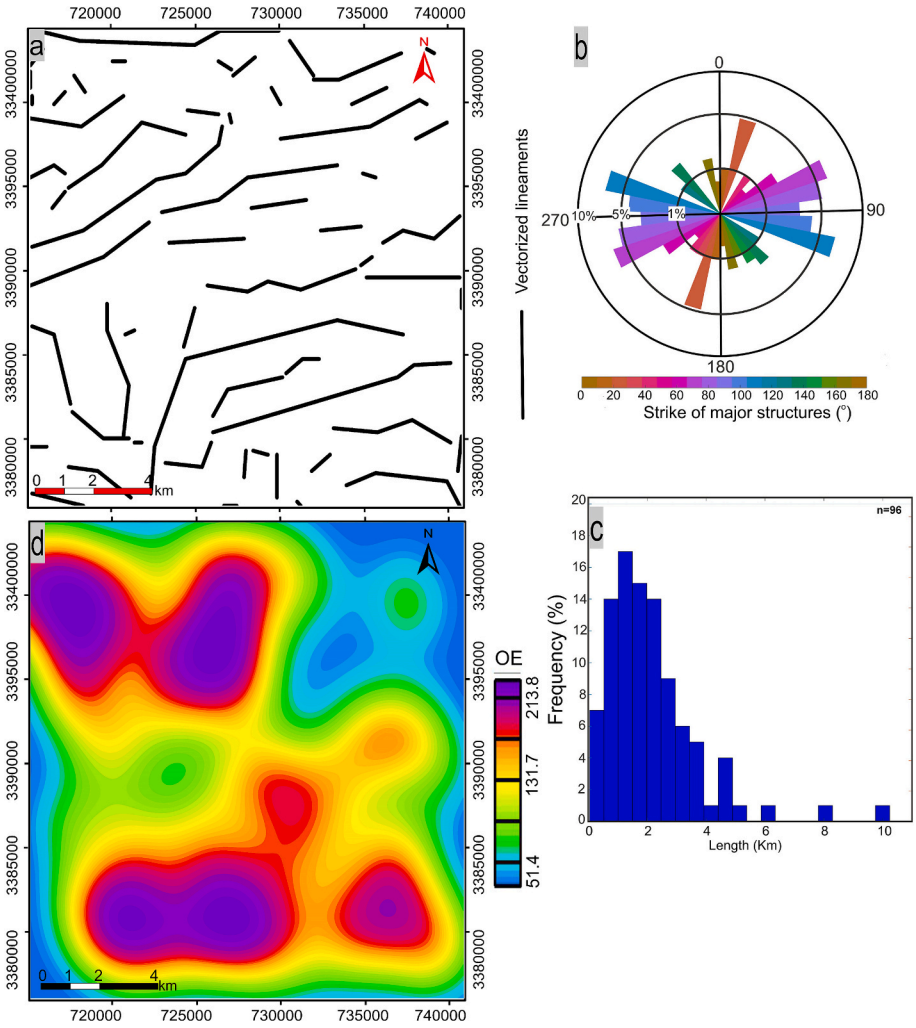


Fig. 12. CET results a) Vectorization lineaments map, b & c) Statistical analysis of lineaments via rose and histogram diagrams, d) Orientation entropy heat map.

The Dark Object Subtraction (DOS) algorithm was applied for atmospheric correction to minimize aerosol influence and obtain accurate surface reflectance values (Chavez, 1996). Spectral values were then normalized to ensure quantitative analysis. Finally, the images were reprojected to the UTM Zone 29 N coordinate system (WGS 84, EPSG:32629) and resampled to a 10 m resolution to ensure spatial consistency.

The following indices are calculated to detect the targeted minerals:

All indices were computed using Python 3.10 with GDAL 3.6.2 for array operations, then imported to QGIS 3.36.0 and Sufer 29.0.250 for visualization

4.1.2. PRISMA image processing

PRISMA hyperspectral data (L2D), available since 2019, offer high spectral resolution, enabling detailed characterization of minerals and hydrothermal alterations. PRISMA provided high-resolution spectral data spanning the visible and near-infrared (VNIR) region (66 bands from 400 to 1100 nm) and the shortwave infrared (SWIR) region (174 bands from 920 to 2500 nm), and we incorporated all of these bands into our analysis. To fully exploit these data, several advanced techniques have been applied. Independent Component Analysis (ICA) was used to separate spectral sources and identify independent components related to target minerals (Gholami et al., 2012; Pour et al., 2019). This method is particularly effective in reducing noise and revealing fine details often masked in hyperspectral data. The ICA analysis was performed using the full PRISMA dataset, resulting in approximately 240 independent components (ICs). A subset of ICs was selected based primarily on visual interpretation, guided by the geological context of the study area. Components that most clearly enhanced lithological boundaries and structural features were prioritized and presented in our results. Next, the Sequential Maximum Angle Convex Cone (SMACC) modeling approach was employed to progressively identify spectral endmembers—i.e., the pure spectral signatures of materials—and map their distribution within the image (Aggarwal and Garg, 2015). SMACC can be considered a spectral unmixing method. We have applied this technique as it is particularly effective in regions with spectrally mixed pixels, allowing for the identification and quantification of individual endmembers. This approach enhances the accuracy of mineral and lithological mapping, especially in complex geological settings where pixel values represent mixtures of multiple materials. While applying ICA for data reduction and then using the independent components as inputs for SMACC is a valid approach, we conducted several experiments, including this method. However, in this study, we decided to utilize the full PRISMA dataset for all analyses (including SMACC) to ensure that we extracted the maximum amount of information from the data. By prioritizing the use of the full dataset, we were able to capture a comprehensive view of the lithological and mineralogical features of the study area. While some noisy bands and outputs were present, a thorough visual interpretation was performed to accurately depict the detailed characteristics of the study area. This approach is well-suited for hyperspectral data, where strong correlations between channels and pixels can complicate the analysis. SMACC simplifies this

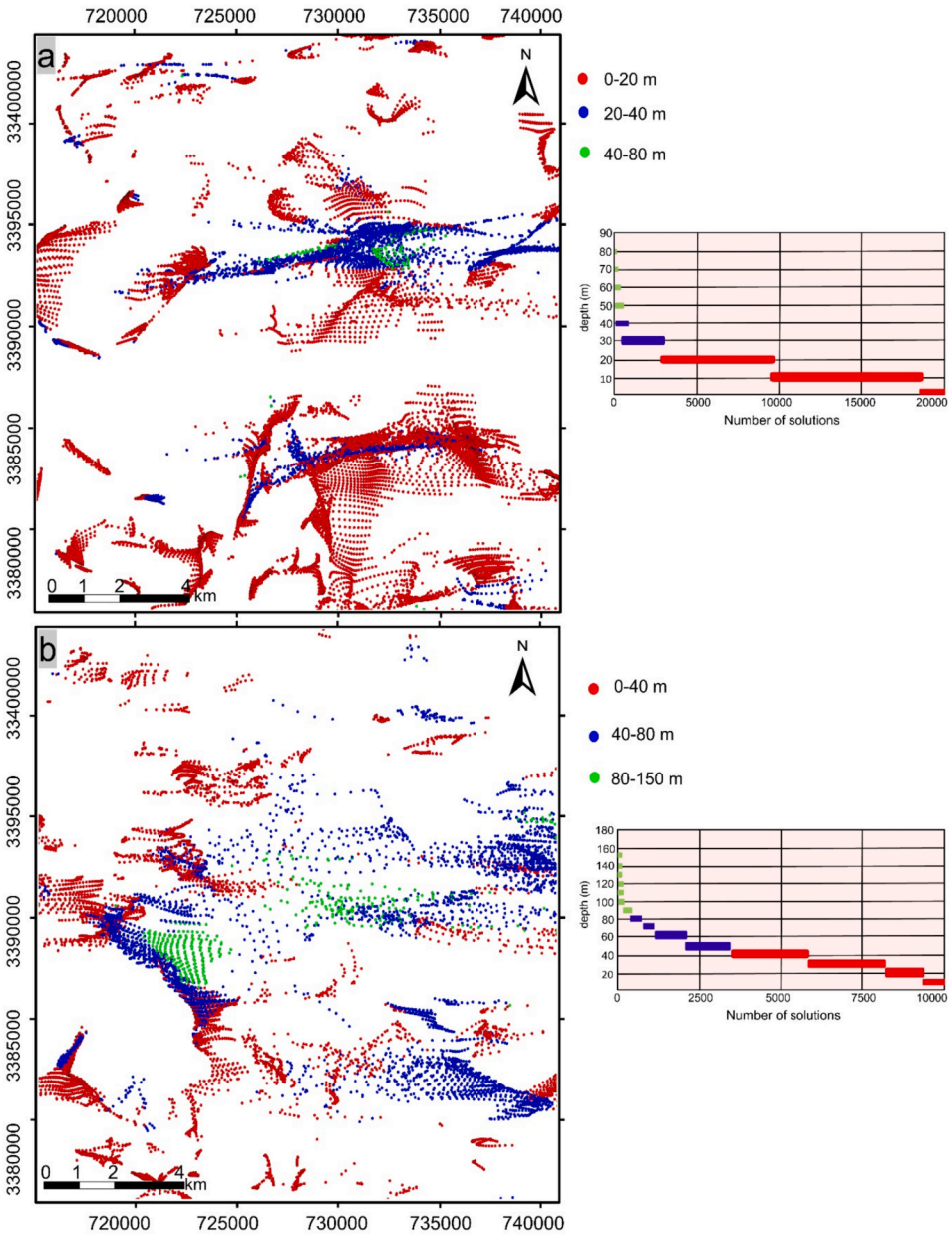


Fig. 13. Euler depths: (a) Depth solutions of the contact model, (b) Depth solutions of the fault model, complemented by a statistical analysis of the depth solutions to accurately define the depth range limits.

complexity and accurately pinpoints areas rich in specific minerals. The SMACC algorithm was applied using 30 endmembers, while all other parameters were retained at their default settings. Finally, the Constrained Energy Minimization (CEM) method was applied to enhance spectral signals associated with target minerals while minimizing background noise interference (Pour et al., 2019; Shebl et al., 2021). This technique is particularly useful for identifying minerals related to hydrothermal alterations, aiding in the selection of the most promising areas for exploration. By combining these techniques, we can maximize the potential of PRISMA hyperspectral data, transforming complex spectral information into clear and actionable results for geological mapping and mineral exploration.

4.2. Aeromagnetic data processing

The data processing of aeromagnetic measurements involved Reduction to the Magnetic Pole (RTP) to reposition magnetic anomalies over their sources (Baranov and Naudy, 1964), applying a declination of −4.5° and an inclination of 41.9° (Fig. 3). The First Vertical Derivative (FVD) (Cooper and Cowan, 2004)was used to enhance local anomalies and delineate lithological contacts, while the Theta map facilitated the identification of geological structures such as faults and dykes (Wijns et al., 2005). The Centre for Exploration Targeting (CET) (Holden et al., 2012)analysis was applied for automatic detection of lineaments and magnetic ridges, highlighting mineralization-prone areas. Finally, Euler deconvolution was utilized to estimate the depths of magnetic sources (Reid et al., 1990), employing structural indices of 0 (contacts) and 1 (faults).

4.3. Field sampling and preparation of polished sections

To complement the study, field missions were conducted to validate the results obtained through remote sensing and geophysical methods. During these missions, sampling was carried out across all types of

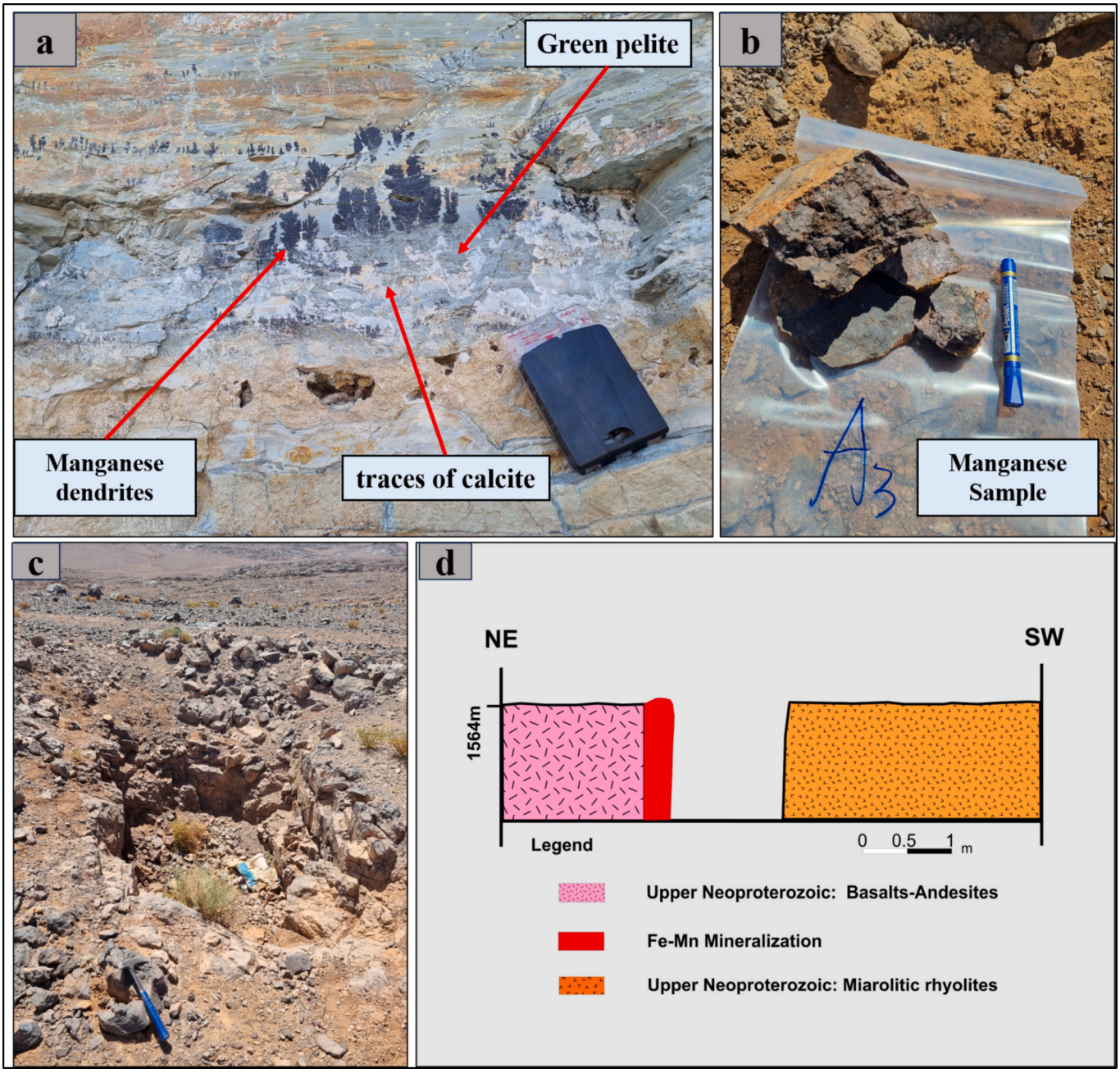


Fig. 14. (a) Manganese dendrites on green pelites with traces of calcite, (b) Manganese sample collected from the field, (c) Trench exposing Fe-Mn mineralization hosted in miarolitic rhyolites and basalt-andesites, (d) Geological cross-section of trench (c) showing the distribution of lithological units and mineralization. (For interpretation of the references to color in this figure legend, the reader is referred to the web version of this article.)

mineralization observed in the field. These samples were then prepared as polished sections to enable detailed microscopic analysis. The preparation of polished sections allows for the examination of mineral textures, associations, and compositions at a microscopic scale, providing critical insights into the mineralogical characteristics and helping to refine the interpretation of the mineralization processes.

5. Results

5.1. Sentinel 2 results

5.1.1. Copper

The analysis of the copper anomaly map highlights a structured distribution of concentrations, strongly influenced by regional geology and tectonic structures. High-anomaly zones are primarily located along major faults and within lithological formations conducive to mineralization (Fig. 4.a).

The most pronounced anomalies are observed in the volcanosedimentary formations (NP3, NP2, and m2-3), which are rich in mafic and ultramafic rocks—environments favorable to copper mineralization. Additionally, formations of the Ouarzazate Group (PIII, m2) exhibit significant indicators, likely associated with hydrothermal alterations linked to tectonomagmatic events.

The spatial organization of anomalies suggests a strong structural control, with mineralization concentrated along faults and shear zones. This pattern indicates that copper mineralization results from the circulation of metal-rich hydrothermal fluids, which precipitate within predisposed lithologies.

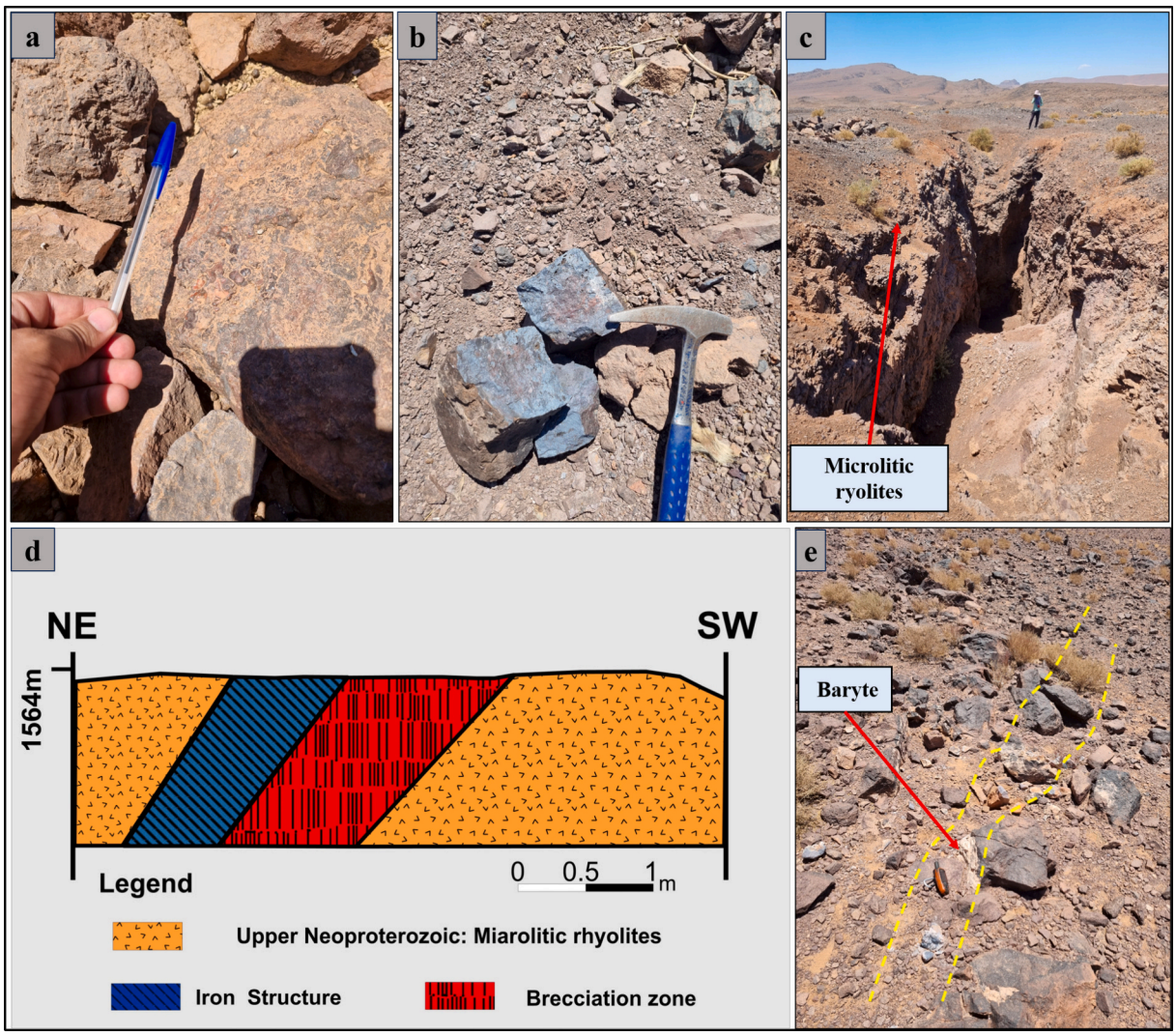


Fig. 15. (a) Hematite, (b) Iron sample, (c) Trench exposing iron mineralization hosted in rhyolites, (d) Cross-section of a trench showing an iron-bearing structure, (e) Baryte structure hosted in andesites.

Certain anomalies have been detected within sedimentary formations (m2 and qle), suggesting possible metal remobilization or secondary enrichment processes. Further analysis is required to determine the nature and origin of these mineralizations.

From an exploration perspective, priority areas are those where copper anomalies coincide with active tectonic structures and favorable lithologies. These sectors warrant further investigation, including sampling, geophysical surveys, and exploratory drilling. If confirmed through geochemical analyses and field observations, these anomalies could indicate potentially exploitable deposits, refining copper exploration strategies in the region.

5.1.2. Manganese

The interpretation of the manganese anomaly map, overlaid with the geological map, allows for the identification of target zones for mineral exploration. The primary anomalies are concentrated in the northern portion of the study area, with a few isolated occurrences in the south (Fig. 4.b). This distribution suggests elevated manganese concentrations in specific geological formations.

Lithological analysis reveals that these anomalies coincide with the NP3ib and NP2i formations, which consist of volcanic breccias, andesites, and serpentinized formations known for their manganese potential. The relationship between these anomalies and geological structures is also notable, with some concentrations aligning with major regional faults, particularly the Aït Saoun Fault (SW-NE orientation), suggesting hydrothermal fluid circulation as a key factor in mineralization.

To refine these observations, a comparison with geophysical data, particularly magnetic anomaly maps, is essential. Since manganese is often associated with moderate magnetic anomalies, the superimposition of these datasets could enhance target delineation. Additionally, field validation through the identification of mineralized indicators (e.g., gossans, hydrothermal alterations).

Based on these findings, two priority target zones emerge:

1. **Northwestern sector** – characterized by a high density of anomalies associated with NP3ib formations, making it a primary exploration target.
2. **Southwestern sector** – exhibiting scattered anomalies related to tectonic contacts, warranting further geophysical investigations.

5.1.3. Cobalt

The application of spectral indices to Sentinel-2 imagery has identified several potential cobalt anomalies, primarily located within Neoproterozoic ultramafic and serpentinized formations (NP2i), which are known for their cobalt potential (Fig. 5a). These anomalies appear to align with major tectonic structures, suggesting a structural control on mineralization. The superimposition of cobalt anomalies with iron and manganese maps indicates a potential interaction with iron oxides and

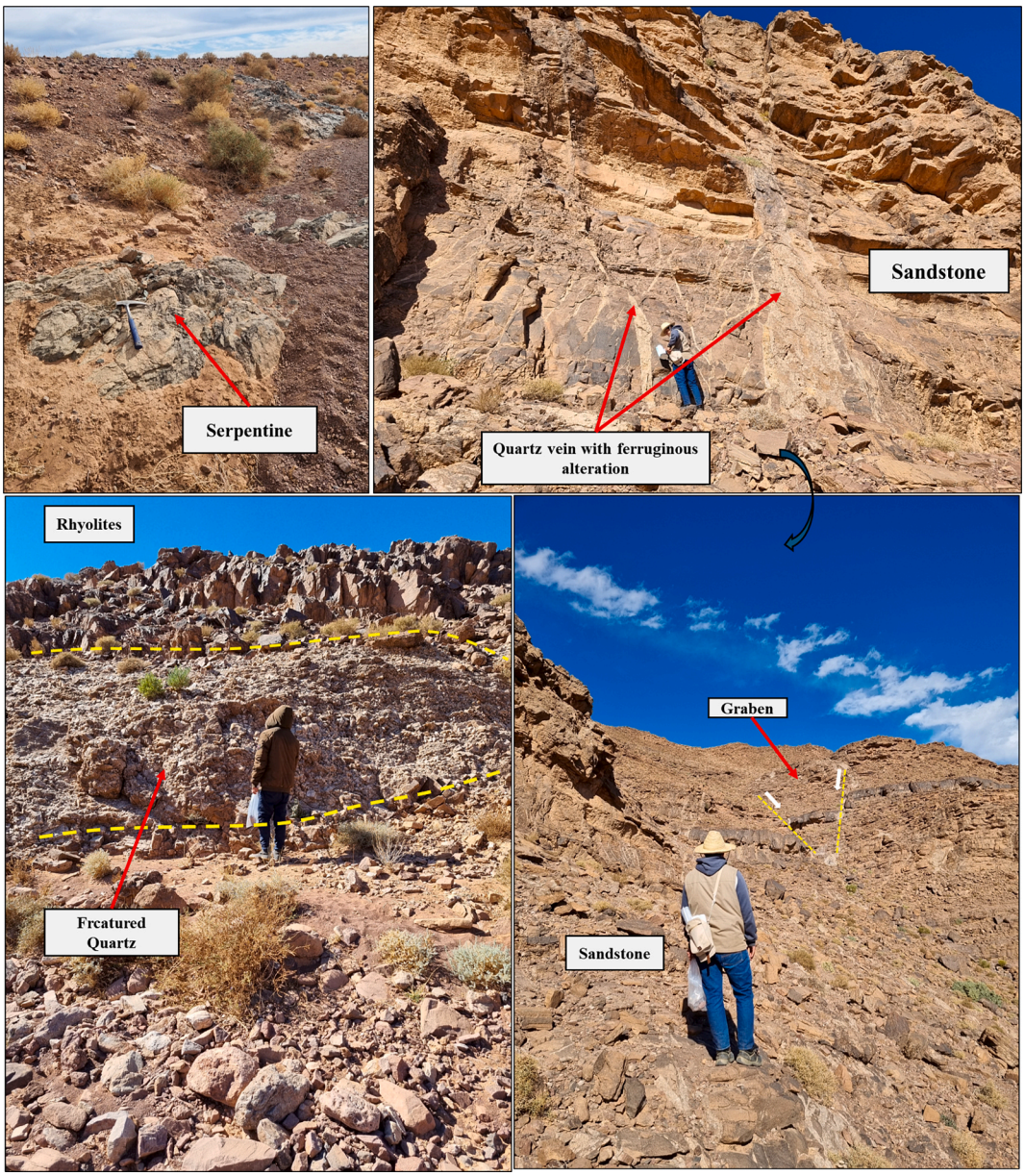


Fig. 16. Lithological and structural features observed in the area: Sandstone units with quartz veins showing ferruginous alteration, intercalated with rhyolites and serpentinized zones.

manganese-bearing minerals.

Certain anomalies are located outside of previously known mineralized zones, potentially revealing new exploration targets. However, the limited spectral resolution of Sentinel-2 prevents precise discrimination of cobalt from associated minerals, and the spatial resolution (10–20 m) may introduce spectral mixing effects. Consequently, validation using hyperspectral data (PRISMA) and field analyses is recommended to confirm these findings.

5.1.4. Baryte

The superimposition of Baryte anomalies with the geological map reveals significant spatial trends in the distribution of this mineralization within the study area. The primary anomalies are concentrated in the southern part of the map, aligning with major geological structures and specific formations (Fig. 5b). This distribution suggests a close relationship between the Baryte anomalies and the Upper Neoproterozoic volcanosedimentary formations (NP3ib), as well as certain units of the Ouarzazate Group (m2, mla). These results are consistent with the observations made in the study of Baryte detection through remote sensing and gravity investigations in Neoproterozoic rocks of the Ariab area, Red Sea Hills, Sudan (Daoud et al., 2025).

The anomalies are particularly pronounced along tectonic contacts and regional faults oriented SW-NE and WNW-ESE, especially in the southern zone, where NP3ib and NP2S formations are in contact with the metasiltstone units of m2. This geological context is conducive to Baryte precipitation in hydrothermal environments, where fluid circulation along fractures plays a crucial role. Furthermore, the presence of hydrothermal alterations within these formations, often associated with Baryte mineralization, suggests localized enrichment in barium sulfates.

5.1.5. Iron

The analysis of spectral indices applied to Sentinel-2 data has identified zones with high concentrations of iron oxides (hematite, goethite), appearing as distinct anomalies on the map (Fig. 6).

These anomalies are primarily associated with the Ouarzazate Group formations (PIII) and units rich in hydrothermal alteration, confirming

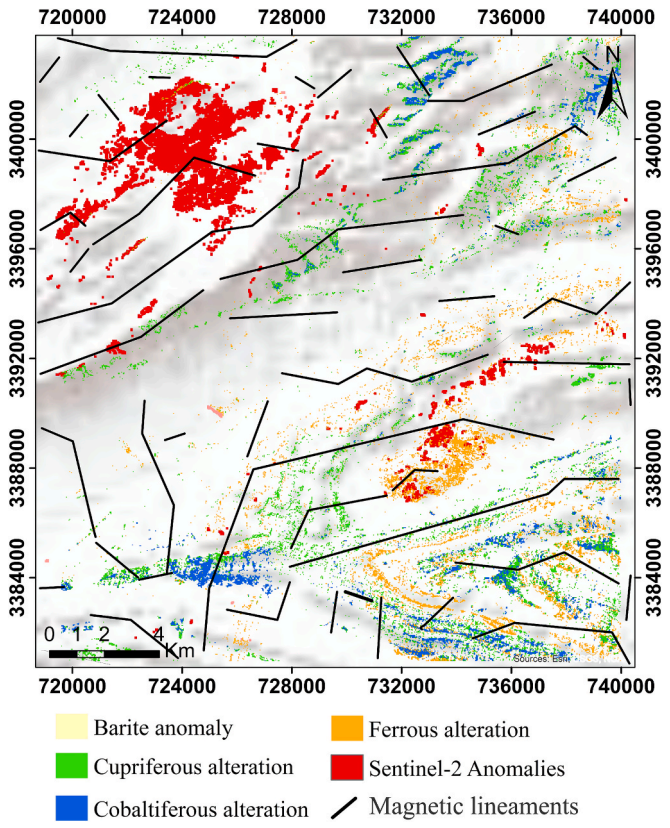


Fig. 17. Final composite map illustrating the spatial relationship between NE–SW trending tectonic lineaments (derived from aeromagnetic data) and remote sensing-detected hydrothermal alteration anomalies, highlighting structurally controlled zones with potential for mineralization.

their correlation with environments favorable for iron mineralization. However, the use of Sentinel-2 data presents certain limitations. The relatively low spectral resolution in the SWIR and Red bands does not allow for optimal discrimination between iron oxides and other types of alteration, such as argillization or silicification. As a result, although the general distribution patterns of iron are consistent with expected geological models, these findings should be interpreted with caution and ideally supplemented by hyperspectral analyses (PRISMA) and field validation.

5.2. *PRISMA data findings*

The remote sensing investigations using PRISMA hyperspectral data have revealed that the study area is lithologically-complex. This analysis sheds light on key formations that could potentially be mineralized zones, aiming to discriminate them effectively and link them with the previous Sentinel-2 findings. To achieve better characterization of the rock units and separation of spectrally similar zones, SMACC endmember analysis was applied to PRISMA hyperspectral data.

Fig. 7a shows the Endmember 2 abundance map, which reveals three main zones with almost identical spectral responses, represented by dark brown coloration. These zones are primarily located in the northwestern, southwestern, and central-eastern parts of the study area. Detailed investigations indicate that the first zone corresponds to the NP3 formation, characterized by heterogeneous lithologies, including conglomerates, volcanic breccias, rhyolitic volcanic tuffs, rhyolites, and andesites. The gradual color variation from light brown to dark brown highlights the intensity of hydrothermal alteration processes, which may be influenced by lithological variations within the district. The second zone, located in the southern part of the study area, corresponds to the NP2 formation, which comprises metamorphosed and foliated basic and ultrabasic magmatic rocks. These rocks are associated with folded and metamorphosed volcano-sedimentary formations formed during the first phase of the Pan-African orogeny. The main similarity between the first and second zones is their depiction of iron-bearing alterations or iron-mineral-rich rocks, as evidenced by the volcano-sedimentary associations and basic-ultrabasic lithologies. The third zone, represented by argillic and sandstone lithologies, is interpreted based on its iron content, which acts as a cementing material. This research identifies Endmember 2 abundance as indicative of iron-bearing rocks within the study area. This conclusion is further supported by the distribution of scattered brown pixels in the central part of the study area and along the NE-SW trending lithologies of the terrain. Variations in the spectral characteristics of these zones and their associated hydrothermal alterations are more effectively visualized using the pseudocolor ramp in Fig. 7b and 8a (Endmembers 3 and 9). The ramp transitions (Fig. 7b) from violet to green-yellow to brown, as observed and represented in the western art of the study area.

In addition to SMACC, independent component analysis was performed on the hyperspectral data to reduce noise and redundancy while extracting useful information. This analysis revealed a distinct zone in the northwestern part of the study area, which is visually distinguished from other lithologies and represented in red in Fig. 8b. The investigations identified this zone as predominantly highlighting NP3 rocks in the northern part of the study area. Further examination of Fig. 8b shows several discrete red pixels in the western and southern parts of the study area. Upon conducting a spatial overlay analysis with the geological map and corroborating with our field observations, these pixels were found to mainly represent NP2 and NP3 formations. These formations constitute the principal lithologies associated with hydrothermal alterations and mineralization within the studied terrain. This analysis is typically-coinciding with the anomalies highlighted by Sentinel 2 data for Cobalt, Manganese and baryte.

Further analysis of hydrothermally altered zones was conducted using IC3 (Fig. 9a), which revealed three main zones within the studied terrain: The northwestern zone, a NE–SW trending zone, and a southwestern zone are all distinguished by dark brown coloration in Fig. 7a. While some scattered pixels may represent noise or false positives, this endmember combination was selected due to the clear prominence and continuity of the main trends, which stand out distinctly despite the presence of minor spectral noise. These zones are primarily hydrothermally altered and highlight the complexity of hydrothermal alterations and their pervasive nature across various lithologies.

For more accurate analysis and interpretation, a widely accepted spectral mapping technique, Constrained Energy Minimization (CEM), was applied to identify the main alteration minerals within the studied terrain and the lithologies hosting potential mineralization. The distribution of these minerals is presented in Fig. 9b, showing a preliminary correlation with the image processing results from Sentinel-2 and PRISMA data. For example, serpentinite minerals, depicted in pink, predominantly coincide with the distribution of ultrabasic rocks that have undergone serpentinization, primarily concentrated in the northern half of the study area. Baryte and chalcopyrite signatures appear as discrete pixels with limited distribution, which aligns with the localized nature of these minerals. These signatures are sometimes observed in wadi deposits, potentially representing the effects of weathering on the host rocks. Iron oxides, such as hematite, jarosite, and limonite, are primarily observed in the southern parts of the study area, with minor discrete pixels scattered throughout. Hydroxyl-bearing minerals, such as malachite, are represented by yellow pixels and are distributed across key zones within the study area.

A comparison of PRISMA findings with Sentinel-2 data results revealed a general agreement in identifying the northwestern and southwestern parts of the study area as highly altered zones. These zones are primarily enriched with iron, manganese (Mn), and hydroxyl (OH)-bearing minerals, along with discrete pixel distributions in the central part of the study area. For example, the manganese distribution map

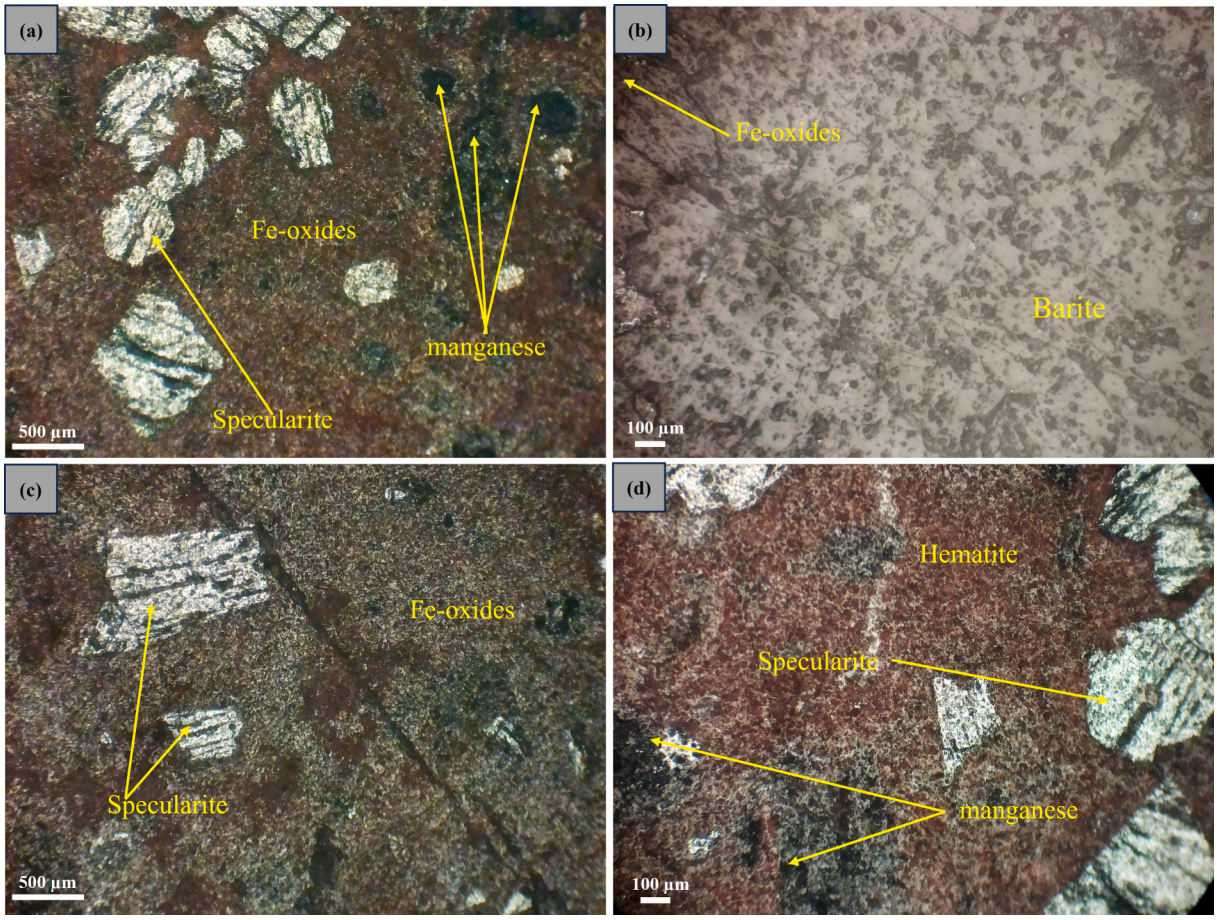


Fig. 18. Microscopic observations of metallic mineralization in host rocks. Manganese and iron oxide mineralization observed in a Neoproterozoic andesite (a), Baryte hosted in andesites (b), iron mineralization associated with rhyolites (c), and manganese-iron association in a Neoproterozoic andesite (d).

derived from Sentinel-2 data, represented by red pixels, aligns closely with the IC11 results from PRISMA data. These findings strongly coincide with the basic and ultrabasic rocks of NP2 and NP3 formations. Similarly, most of iron anomalies detected using Sentinel-2 data are corroborated by PRISMA analyses, including SMACC results (e.g., End-member 2) and the Constrained Energy Minimization (CEM) method. The slight variation between the Sentinel-2 iron anomalies and the hematite distribution derived from PRISMA using the CEM method can be explained by several factors. Firstly, the iron index from Sentinel-2 represents range of iron-bearing minerals, including both hematite and goethite, and is not limited to hematite alone. This may account for the relatively varied distribution of anomalies observed in the Sentinel-2 results. Secondly, a closer examination of the southeastern part of the study area reveals areas where hematite-rich zones identified by CEM do overlap with the Sentinel-2 iron index, supporting consistency in certain regions. Moreover, the CEM was applied using a strict threshold to minimize noise and enhance specificity, which naturally constrained the spatial extent of highlighted hematite pixels. Together, these considerations reflect the complementary strengths of multispectral and hyperspectral datasets in mineral mapping. Furthermore, copper and cobalt bearing mineral distributions identified through Sentinel-2 data align well with the malachite distribution mapped using PRISMA data through the CEM and Independent Component Analysis (ICA) methods.

5.3. Aeromagnetic data

For enhancing local anomalies in the area, highlighting lithological contacts and helping outline the edges of anomalous bodies from the data, the first vertical derivative and theta maps (Fig. 3) was routinely computed from the RTP data. The FVD map shows that most of the short-wavelength anomalies were located in the western part. The major trend in this map is the NE-SW direction with the other associated trends in the NW-SE, E-W and N-S directions. More abundant structures can be observed from the theta map (Fig. 10).

In the other hand, the automated detection of lineaments in terms of ridge structures are revealed by applying the CET grid analysis approach. Preliminary Standard deviation (Fig. 11) features the magnetic discontinuity parts and used as the input grid for detecting laterally line-like zones represented by white color in the PS map (Fig. 11a), then through a thresholding filter reduce these zones into skeletal structures appeared as cyan color. To end up with the vectorization process for producing lineament-based ridges (Fig. 12 a). The area is highly deformed, and the structural features are oriented in NE-SW, NW-SE, N-S and E-W directions. Statistical analysis of these detected lineaments has been carried via rose and histogram diagrams (Fig. 12b & c).

The variation in orientation of the detected features could be converted into a complexity heat map in terms of orientation entropy (Fig. 12d), exhibiting the optimistic zones of mineral occurrences. The depths of the estimated features as contacts and faults are estimated by applying Euler deconvolution approach with structure index 0 and 1, respectively. Assuming contact and fault models with a moving window of 5 × 5 data points and a 3 % relative inaccuracy. The source location is represented by circular symbols revealing the estimated depth values, which range from 0 to a little more than 80 m and 150 m in both contact and faults (Fig. 13), indicating shallow magnetic sources.

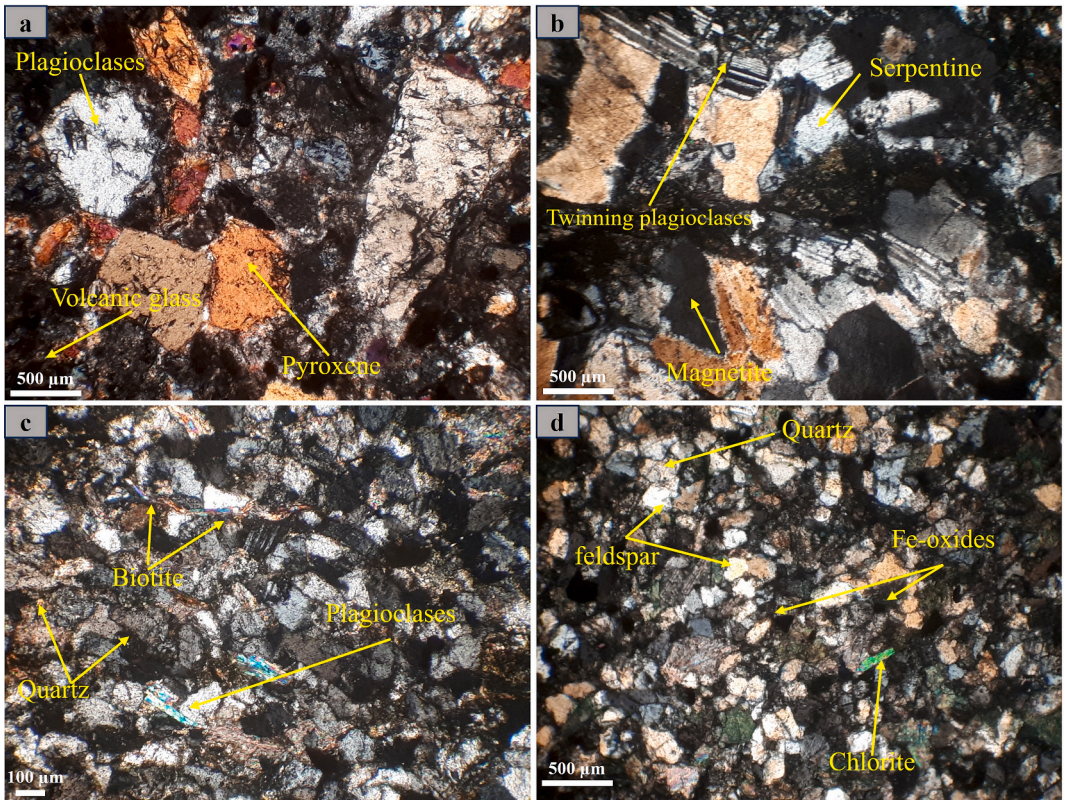


Fig. 19. Thin Section Observations of Volcanic and Sedimentary Rocks: a) Basalt, b) Serpentinite, c) Sandstone, d) rhyolite.

5.4. Validation and Evaluation

To validate and evaluate the results obtained from remote sensing and geophysical analyses, field verification missions were conducted across the study area. These missions aimed to assess the accuracy of the identified mineralization zones and to collect representative samples from various lithological units and alteration zones (Fig. 14).

During these campaigns, samples were systematically collected from locations corresponding to high-anomaly zones for copper, manganese, cobalt, Baryte, and iron, as identified by Sentinel-2 and PRISMA data. Emphasis was placed on areas where spectral and magnetic anomalies aligned with major tectonic features—such as faults and shear zones—identified through visual overlay analysis in QGIS. This approach, was selected to directly interpret spatial correlations based on expert geological knowledge, especially where structural controls on mineralization are well established (Fig. 15).

Field observations in the graben structure reveal alternating sandstone and rhyolite units, cross-cut by quartz veins with prominent ferruginous alteration (Fig. 16). The presence of fractured quartz and serpentine suggests localized fluid circulation along fault zones, consistent with the hydrothermal mineralization model proposed. Subsequently, a finalized composite map (Fig. 17) was generated through spatial overlay analysis, integrating remote sensing-derived hydrothermal alteration anomalies with structural features interpreted from aeromagnetic data. This analysis revealed a predominant NE–SW trend of tectonic lineaments spatially associated with the distribution of hydrothermal alteration zones, indicating a structurally favorable setting for potential mineralization within the study area.

The collected samples were prepared as polished thin sections to enable detailed microscopic analysis (Figs. 18 and 19). This process allowed for the identification of mineral textures, associations, and compositions, providing critical insights into the mineralogical characteristics of the study area. For instance, samples from copper-rich zones revealed the presence of malachite, while manganese-rich zones exhibited pyrolusite and psilomelane. Cobalt anomalies were associated with cobaltite and erythrite, and baryte-rich zones confirmed the presence of barium sulfates. Iron anomalies were validated by the identification of hematite and goethite. These findings corroborated the remote sensing and geophysical results, confirming the presence of mineralization in the predicted zones.

The microscopic analysis also provided valuable information on the host rocks and the nature of hydrothermal alterations. For example, the NP3 and NP2 formations, identified as favorable environments for mineralization, showed evidence of intense hydrothermal activity, such as serpentinization and argillic alteration. The integration of field observations with remote sensing and geophysical data significantly enhanced the reliability of the exploration model, reducing uncertainties and refining the interpretation of mineralization processes.

6. Discussion

The integration of remote sensing (Sentinel-2 & PRISMA) and aeromagnetic data has provided a comprehensive understanding of mineralization patterns in the study area. The results reveal strong spatial correlations between spectral anomalies, lithological formations, and structural features, highlighting the geological controls on mineral distribution.

The analysis of Sentinel-2 spectral indices demonstrates a clear alignment of copper, manganese, and cobalt anomalies with major tectonic structures detected through magnetic data analysis. Copper mineralization is predominantly associated with volcanosedimentary formations (NP3, NP2, m2-3) and Ouarzazate Group formations (PIII, m2), suggesting hydrothermal fluid circulation along faults and shear zones. Similarly, manganese anomalies concentrate within NP3ib and NP2i formations, with a notable structural control exerted by the Aït Saoun Fault. These results emphasize the role of regional fault networks in channeling mineralizing fluids. Cobalt anomalies, detected within Neoproterozoic ultramafic and serpentinized formations (NP2i), further

validate this structural control. The overlap of cobalt indices with iron and manganese anomalies suggests potential co-mineralization or secondary enrichment processes. However, Sentinel-2's spectral limitations necessitate validation using hyperspectral data.

PRISMA hyperspectral data analysis enhanced both lithological mapping and hydrothermal alteration detection. Spectral Mixture Analysis using the SMACC algorithm revealed three primary zones with distinct spectral responses, corresponding to NP3, NP2, and clay-sandy units. These zones exhibit strong ferric alterations and hydrothermal processes, as indicated by variations in abundance maps. Independent Component Analysis (ICA) identified a distinct lithological unit in the northwestern region, predominantly composed of NP3 rocks. The Constrained Energy Minimization (CEM) method successfully detected key hydrothermal alteration minerals, including serpentine, baryte, chalcopyrite, and iron oxides, further corroborating the Sentinel-2 results. The integration of PRISMA and Sentinel-2 datasets significantly improved the accuracy of mineralogical mapping and the delineation of hydrothermal alteration zones.

Aeromagnetic data revealed a highly deformed structural framework characterized by NE-SW, NW-SE, E-W, and N-S trending magnetic anomalies. Reduction to the Pole (RTP) and First Vertical Derivative (FVD) maps highlighted short-wavelength anomalies in the western part of the study area, suggesting the presence of shallow magnetic sources. Structural analysis using the Theta map and CET grid method enabled the characterization of key geological features such as faults, contacts, and dykes, which play a critical role in mineralization control. Euler Deconvolution estimated the depth of these structures to range between 0 and 150 m, confirming the presence of shallow magnetic sources. These findings provide crucial insights into the structural controls of mineralization and underscore the importance of integrating aeromagnetic data with remote sensing and geochemical analyses.

The integration of Sentinel-2, PRISMA, and aeromagnetic data has established a robust framework for mineral exploration within the study area. The strong correlation between spectral anomalies, magnetic anomalies, and tectonic structures highlights the value of multisource data fusion for mineral prospecting. Three key observations emerge from this study: (i) mineralization is strongly controlled by tectonic structures, particularly faults and shear zones, which act as conduits for hydrothermal fluids, (ii) favorable lithologies, such as mafic and ultramafic rocks, play a crucial role in hosting mineralization, and (iii) hydrothermal processes are a major factor in mineral deposit formation, as evidenced by the distribution of alteration minerals and their association with tectonic structures.

Future research should address these challenges by focusing on three key aspects: (i) systematic field validation through extensive geological surveys and geochemical sampling to strengthen anomaly confirmation, (ii) expanded remote sensing analysis using commercial data for better spatial (up to 1–3 m pixel size, e.g., WorldView-3 and Planetscope) and spectral characterization for the mineralized zones, and (iii) additional geophysical investigations, such as Induced Polarization (IP) and Electromagnetic (EM) methods, to better delineate mineralization zones. The integration of these multidisciplinary approaches will not only enhance exploration efficiency but also contribute to a more comprehensive understanding of the region's mineral resource potential.

7. Conclusion

Remote sensing investigations have revealed significant copper mineralization potential in the northern and southern parts of the study area. Cobalt and manganese anomalies were detected within Neoproterozoic ultramafic and serpentinized formations (NP2i) as well as in volcanic-sedimentary units (NP3). Baryte and iron oxide anomalies were also identified, with baryte occurrences primarily associated with hydrothermal alterations along tectonic contacts. These anomalies are predominantly controlled by NE-SW, NW-SE, E-W, and N-S trending tectonic structures, as indicated by the regional geological setting. These structural trends were extracted through magnetic data analysis, which revealed a highly deformed and complex fault network. The circulation of hydrothermal fluids along these fault systems played a crucial role in mineralization processes, as evidenced by the alignment of spectral anomalies with major tectonic features.

Field investigations and petrographic analyses confirmed the presence of mineralization in the predicted zones. Microscopic observations identified key mineralogical associations, including malachite for copper, pyrolusite for manganese, cobaltite for cobalt, hematite for iron, and baryte. This integrated approach has proven effective in characterizing the spatial distribution of mineralization and enhancing the understanding of the regional geological framework.

This study underscores the significance of a multidisciplinary approach that combines remote sensing, geophysical analysis, and field validation for efficient mineral exploration in structurally complex settings. To further optimize exploration efforts, the use of higher-resolution hyperspectral data would improve mineral discrimination and mapping accuracy. Additionally, advanced geophysical surveys, such as Induced Polarization (IP) and Electromagnetic (EM) methods, would provide deeper insights into subsurface mineralization. Systematic field validation through geochemical sampling and mineralogical analyses is also essential to refine anomaly interpretation and assess the economic potential of identified targets. This research provides a robust methodological framework for future studies aiming to enhance exploration strategies and mineral resource management in the Aït Semgane region and similar geological environments.

Declaration of competing interest

The authors declare that they have no known competing financial interests or personal relationships that could have appeared to influence the work reported in this paper.

Data availability

Data will be made available on request.

References

Abdelkareem, M., Bamousa, A.O., Hamimi, Z., Kamal El-Din, G.M., 2020. Multispectral and RADAR images integration for geologic, geomorphic, and structural investigation in southwestern Arabian Shield, Al Qunfudhah area, Saudi Arabia. J. Taibah Uni. Sci. 14, 383–401. https://doi.org/10.1080/16583655.2020.1741957.

Ali, A.A., Choukrad, J., Ouahzizi, Y., Charroud, M., Mhamdi, H.S., Saoud, N., Mounir, S., Mechaqrane, A., 2025. Integrated remote sensing and field data for lithological mapping and calcite exploration in the Middle Atlas, Morocco. Sci. Afr. 27, e02521. https://doi.org/10.1016/j.sciaf.2024.e02521.

Ait Ali, A., Charroud, M., Choukrad, J., Ouahzizi, Y., Si Mhamdi, H., El Moutaouakkil, N., Saoud, N., Mechaqrane, A., 2024. Identification, Characterization, and Deposit Model of Calcite Mineralization in the Middle Atlas Belts, Morocco. *Geosciences*. 14 (6), 154. https://doi.org/10.3390/geosciences14060154.

Adiri, Z., El Harti, A., Jellouli, A., Lhissou, R., Maacha, L., Azmi, M., Zouhair, M., Bachaoui, E.M., 2017. Comparison of Landsat-8, ASTER and Sentinel 1 satellite remote sensing data in automatic lineaments extraction: A case study of Sidi Flah-Bouskour inlier, Moroccan Anti Atlas. Adv. Space Res. 60, 2355–2367. https://doi.org/10.1016/j.asr.2017.09.006.

Aggarwal, A., Garg, R.D., 2015. Systematic approach towards extracting endmember spectra from hyperspectral image using PPI and SMACC and its evaluation using spectral library. Appl Geomat 7, 37–48. https://doi.org/10.1007/s12518-014-0149-5.

Ali EL-Omairi, M., El Garouani, A., Shebl, A., 2024. Investigation of lineament extraction: Analysis and comparison of digital elevation models in the Ait Semgane region, Morocco. Remote Sens. Appl.: Soc. Environ. 36, 101321. https://doi.org/10.1016/j.rsase.2024.101321.

Aplin, P., 2004. Remote sensing: land cover. Prog. Phys. Geogr.: Earth Environ. 28, 283–293. https://doi.org/10.1191/0309133304 pp413pr.

Bajja, A., 1987. Nouvelles données pétrographiques et géochimiques sur les formations volcaniques précambriennes du Djebel Saghro (anti-atlas marocain), basaltes en coussins du P II et volcanites de la série de Ouarzazate (P III).

Baranov, V., Naudy, H., 1964. numerical calculation of the formula of reduction to the magnetic pole. Geophysics 29, 67–79. https://doi.org/10.1190/1.1439334.

Bedini, E., 2017. The use of hyperspectral remote sensing for mineral exploration: a review. Jour. Hypers. Rem. Sensg. 7, 189–211. https://doi.org/10.29150/jhrs.v7.4.p189-211.

Blein, O., Razin, P., Chevremont, P., Baudin, T., Gasquet, D., Abderrahmane, S., Admou, H., Youbi, N., Bouabdelli, M., Anzar, C., 2011. Notice explicative carte géologie Maroc (1/50,000), feuille d'Alougoum. Notes and Mémoires Service Géologique Maroc.

Chavez, P.J., 1996. Image-Based Atmospheric Corrections - Revisited and Improved. Photogramm. Eng. Remote Sens. 62, 1025–1036.

Cooper, G.R.J., Cowan, D.R., 2004. Filtering using variable order vertical derivatives. Comput. Geosci. 30, 455–459. https://doi.org/10.1016/j.cageo.2004.03.001.

Choukrad, J., Ouahzizi, Y., Ali, A.A., Charroud, M., 2022. Geology, mineralogy, geochemistry and deposit model of iron and manganese in Bouarfa mine, Eastern High Atlas, Morocco. Sci. Afr. 18, e01401. https://doi.org/10.1016/j.sciaf.2022.e01401.

Daoud, A.M.A., Shebl, A., Abdelkader, M.M., Mohieldain, A.A., Csámer, Á., Satti, A.M.N., Rózsa, P., 2025. Remote sensing and gravity investigations for barite detection in Neoproterozoic rocks in the Ariab area, Red Sea Hills, Sudan. Remote Sens. Appl.: Soc. Environ. 37, 101416. https://doi.org/10.1016/j.rsase.2024.101416.

EL-Omairi, M.A., El Garouani, A., 2023. A review on advancements in lithological mapping utilizing machine learning algorithms and remote sensing data. Heliyon 9, e20168. https://doi.org/10.1016/j.heliyon.2023.e20168.

El-Omairi, M.A., El Garouani, M., El Garouani, A., 2025. Enhanced lithological mapping via remote sensing: Employing SVM, random trees, ANN, with MNF and PCA transformations. The Egyptian Journal of Remote Sensing and Space Sciences 28, 34–52. https://doi.org/10.1016/j.ejrs.2024.12.001.

Evans, A.M., 2012. Ore geology and industrial minerals: an introduction, 3. ed., 18. [Dr.]. ed, Geoscience texts. Blackwell Publ, Malden.

Gholami, R., Moradzadeh, A., Yousefi, M., 2012. Assessing the Performance of Independent Component Analysis in Remote Sensing Data Processing. J. Indian Soc. Remote Sens. 40, 577–588. https://doi.org/10.1007/s12524-011-0189-9.

Gonzalez-Alvarez, I., Goncalves, M.A., Carranza, E.J.M., 2020. Introduction to the Special Issue Challenges for mineral exploration in the 21st century: Targeting mineral deposits under cover. Ore Geology Reviews 126, 103785. https://doi.org/10.1016/j.oregeorev.2020.103785.

Harben, P.W., Kužvart, M., 1997. Industrial Minerals: A Global Geology. Industrial Minerals Information Limited.

Holden, E.-J., Wong, J.C., Kovesi, P., Wedge, D., Dentith, M., Bagas, L., 2012. Identifying structural complexity in aeromagnetic data: An image analysis approach to greenfields gold exploration. Ore Geol. Rev. 46, 47–59. https://doi.org/10.1016/j.oregeorev.2011.11.002.

Hunt, G.R., Ashley, R.P., 1979. Spectra of altered rocks in the visible and near infrared. Econ. Geol. 74, 1613–1629. https://doi.org/10.2113/gsecongeo.74.7.1613.

Liu, C., Qiu, C., Wang, L., Feng, J., Wu, S., Wang, Y., 2023. Application of ASTER Remote Sensing Data to Porphyry Copper Exploration in the Gondwana Region. Minerals 13, 501. https://doi.org/10.3390/min13040501.

Liu, P., 2015. A survey of remote-sensing big data. Front. Environ. Sci. 3. https://doi.org/10.3389/fenvs.2015.00045.

Maacha, L., Ennaciri, O., Ghorfi, M.E., Saquaque, A., Alansari, A., Soulaimani, A., n.d. 2.4- Le district à cobalt, nickel et arsenic de Bou Azzer (Anti-Atlas central) / 9.

Maynard, J.B., 2012. Geochemistry of Sedimentary Ore Deposits. Springer Science & Business Media.

Mineral Commodity Summaries 2023, 2023.

Moon, E.C.J., Whateley, M.K.G., Evans, A.M., n.d. Introduction to Mineral Exploration.

Mohamed Ez-Zghoudy, Moha Ikenne, Mustapha Souhassou, Mohamed Alaeddine Belfoul, Mohamed Gouiza, Said Ilmen, Mehdi Ousbih, Abdelhak Karfal, Lhou Maacha, Mohamed Zouhair, Structural controls on the Co and Ni-bearing arsenides from the Bou Azzer mine (Case of Aït Ahmane F53 vein deposit): Implications for mineral exploration, Journal of African Earth Sciences, Volume 202, 2023, 104929, ISSN 1464-343X, https://doi.org/10.1016/j.jafrearsci.2023.104929.

Pour, A.B., Park, Y., Park, T.-Y.-S., Hong, J.K., Hashim, M., Woo, J., Ayoobi, I., 2019. Evaluation of ICA and CEM algorithms with Landsat-8/ASTER data for geological mapping in inaccessible regions. Geocarto. International.

Reid, A.B., Allsop, J.M., Granser, H., Millett, A.J., Somerton, I.W., 1990. Magnetic interpretation in three dimensions using Euler deconvolution. Geophysics 55, 80–91. https://doi.org/10.1190/1.1442774.

Riser, J., 1988. Anti-Atlas. Encyclopédie Berbère 776–791. https://doi.org/10.4000/encyclopedieberbere.2522.

Saber Salmi, Ezzoura Errami, Abdellatif Jouhari, Jamal El Kabouri, Nasser Ennih, Omar Outaaoui, Said Ilmen, Younes Moundi, Abdelhak Karfal, Lhou Maacha, Constraints of the regional deformation on the hydrothermal veins in Ousdrat and Aït Ahmane ore deposits (Bou Azzer-El Graara inlier, central Anti-Atlas, Morocco): Implications for mineral exploration, Journal of African Earth Sciences, Volume 220, 2024, 105441, ISSN 1464-343X, https://doi.org/10.1016/j.jafrearsci.2024.105441.

Shaik, R.U., Periasamy, S., Zeng, W., 2023. Potential Assessment of PRISMA Hyperspectral Imagery for Remote Sensing Applications. Remote Sens. (Basel) 15, 1378. https://doi.org/10.3390/rs15051378.

Shebl, A., Abdellatif, M., Badawi, M., Dawoud, M., Fahil, A.S., Csámer, Á., 2023. Towards better delineation of hydrothermal alterations via multi-sensor remote sensing and airborne geophysical data. Sci. Rep. 13, 7406. https://doi.org/10.1038/s41598-023-34531-y.

Shebl, A., Abdellatif, M., Elkhateeb, S.O., Csámer, Á., 2021. Multisource Data Analysis for Gold Potentiality Mapping of Atalla Area and Its Environs, Central Eastern Desert. Egypt. Minerals 11, 641. https://doi.org/10.3390/min11060641.

Shebl, A., Abriha, D., Fahil, A.S., El-Dokouny, H.A., Elrasheed, A.A., Csámer, Á., 2023. PRISMA hyperspectral data for lithological mapping in the Egyptian Eastern Desert: Evaluating the support vector machine, random forest, and XG boost machine learning algorithms. Ore Geol. Rev. 161, 105652. https://doi.org/10.1016/j.oregeorev.2023.105652.

Shebl, A., Kusky, T., Csámer, Á., 2022. Advanced land imager superiority in lithological classification utilizing machine learning algorithms. Arab. J. Geosci. 15, 923. https://doi.org/10.1007/s12517-022-09948-w.

Sillitoe, R.H., 2010. Porphyry Copper Systems. Econ. Geol. 105, 3–41. https://doi.org/10.2113/gsecongeo.105.1.3.

Telford, W.M., Geldart, L.P., Sheriff, R.E., 1990. Applied Geophysics, 2nd ed. Cambridge University Press. https://doi.org/10.1017/CBO9781139167932.

Van Der Meer, F.D., Van Der Werff, H.M.A., Van Ruitenbeek, F.J.A., Hecker, C.A., Bakker, W.H., Noomen, M.F., Van Der Meijde, M., Carranza, E.J.M., Smeth, J.B.D., Woldai, T., 2012. Multi- and hyperspectral geologic remote sensing: A review. Int. J. Appl. Earth Obs. Geoinf. 14, 112–128. https://doi.org/10.1016/j.jag.2011.08.002.

Walsh, G.J., Benziane, F., Aleinikoff, J.N., Harrison, R.W., Yazidi, A., Burton, W.C., Quick, J.E., Saadane, A., 2012. Neoproterozoic tectonic evolution of the Jebel Saghro and Bou Azzer—El Graara inliers, eastern and central Anti-Atlas, Morocco. Precambr. Res. 216–219, 23–62. https://doi.org/10.1016/j.precamres.2012.06.010.

Wijns, C., Perez, C., Kowalczyk, P., 2005. Theta map: Edge detection in magnetic data. Geophysics 70, L39–L43. https://doi.org/10.1190/1.1988184.

Yazidi, A., Benziane, F., Walsh, G., Harrison, R.W., Saadane, A., Yazidi, M., Quick, J., Fahssi, A., Stone, B., Aleinikoff, J., Ejjaouani, H., Kalai, M., 2008. Carte géologique au 1/50 000. Feuille Ait Semgane, Notes et Mémoires du Service Géologique du Maroc, p. 472.